

ACOUSTOOPTICAL TECHNIQUES FOR ULTRASONIC MATERIALS  
EVALUATION:  
OPTICAL FIBER INTERFEROMETRY AND PULSE-ECHO SYSTEMS

by

Janet Christiana Wade

Thesis submitted to the Faculty of the  
Virginia Polytechnic Institute and State University  
in partial fulfillment of the requirements for the degree of  
MASTER OF SCIENCE  
in  
ELECTRICAL ENGINEERING

APPROVED:

-----  
Dr. R. O. Claus

-----  
Dr. C. W. Bostian

-----  
Dr. C. E. Nunnally

May, 1982  
Blacksburg, Virginia

## ACKNOWLEDGEMENTS

I would like to express my gratitude and appreciation to my advisor, Dr R. O. Claus, for his ideas, support, encouragement, and enthusiasm which have made this endeavor possible. I acknowledge the members of my advisory committee, Dr. C. W. Bostian and Dr. C. E. Nunnally, and the entire electrical engineering faculty and staff for their time and instruction during both my undergraduate and graduate studies. I must especially thank the department secretaires, particularly Vicki Trump, for their patience and organization.

I also acknowledge my fellow graduate and undergraduate students in the Acoustooptics Group, Dan Dockery, Avinash Garg, John Gray, Ken Ocheltree, Tyson Turner, and Sam Zerwekh, for their suggestions and help on this project. Also, I would like to thank Dr. J. N. Reddy and Jeff Bennighof of the Engineering Science and Mechanics Department for their help in the theoretical analysis of stresses in plates.

Finally, I would like to express my sincere appreciation and thanks to my family, especially my parents, for their unceasing love and moral support.

This research was sponsored in part by grants from NASA and the National Science Foundation.

## TABLE OF CONTENTS

ACKNOWLEDGEMENTS . . . . . ii

Chapter	page
I. INTRODUCTION . . . . .	1
II. OPTICAL FIBER BASICS . . . . .	5
2.1 Optical Fiber Development. . . . .	5
2.2 Optical Fiber Geometry . . . . .	5
2.3 Optical Fiber Sensors. . . . .	12
III. OPTICAL FIBER INTERFEROMETRY . . . . .	18
3.1 Fiber Interferometer Theory . . . . .	18
3.2 Optical Signal Detection . . . . .	20
3.3 Calibration . . . . .	23
IV. EXPERIMENT . . . . .	27
4.1 Optical Detection of Strain in Two-dimensions . . . . .	28
4.2 Acoustic Emission . . . . .	36
4.2 Application of Multimode Fiber in NDE . . . . .	44
V. OPTICAL FIBER INTERFEROMETRY CONCLUSIONS . . . . .	50
VI. PIEZOELECTRIC TRANSDUCERS IN PULSED ULTRASONIC SYSTEMS . . . . .	54
VII. TRANSDUCER AND ELECTRONIC SUBSYSTEM DESIGN . . . . .	61
7.1 Electrode Design and Fabrication . . . . .	61
7.2 Electronic Pulsing Circuitry . . . . .	62
VIII. OPTICAL DETECTION SYSTEM . . . . .	71
8.1 Feedback Stabilized Michelson Interferometer . . . . .	71
8.2 Feedback Stabilization of the Michelson Interferometer . . . . .	72

IX.	ACOUSTOOPTICAL PULSE-ECHO SYSTEM SUMMARY . . . . .	76
	REFERENCES . . . . .	80
	BIBLIOGRAPHY . . . . .	83
Appendices		page
A.	PREPARING OPTICAL FIBERS FOR USE IN AN INTERFEROMETER . . . . .	84
B.	STRAIN DATA AND CALCULATIONS . . . . .	89
C.	FORTRAN PROGRAM FOR CALCULATING TRANSDUCER VARIABLES . . . . .	92
D.	CHEMICAL ETCHANTS . . . . .	97
	VITA . . . . .	100
	ABSTRACT	

LIST OF TABLES

Table	page
2.2.1. Types of Optical Fibers and Their Characteristics . . . . .	10
4.1.1. Theoretical and Experimental Strain Data . . . .	34
A1.1. Center Ring Locations for a Typical Transducer .	95
A1.2. Firing Sequence Data . . . . .	96

## LIST OF FIGURES

Figure	page
2.2.1. Single Mode Optical Fiber Geometry . . . . .	8
2.2.2. Multimode Optical Fiber Geometry . . . . .	9
2.2.3. Optical Fiber Waveguide Ray Diagram . . . . .	11
2.3.1. Single Fiber Optical Sensor . . . . .	14
2.3.2. Mach-Zehnder Interferometer . . . . .	17
3.3.1. Cantilever Beam Calibration Experiment . . . . .	25
3.3.2. Calibration Curve . . . . .	26
4.1.1. Optical Fiber Interferometric System . . . . .	29
4.1.2. Rectangular Plate with Fiber Matrix Attached . .	30
4.1.3. Partitions Used in Finite Element Analysis Program . . . . .	33
4.2.1. Experimental Configuration for Acoustic Emission . . . . .	40
4.2.2. Embedded Optical Fibers in Other Materials . . .	41
4.2.3. Acoustic Emission Event Detection: Time Domain Response . . . . .	42
4.2.4. Acoustic Emission Event: Frequency Domain Response . . . . .	43
4.2.5. Comparison of Single Mode and Multimode Fiber Data . . . . .	45
4.3.1. Laminated Plastic Sheet With Embedded Multimode Fibers . . . . .	48
4.3.2. Position of Load Prior to Release . . . . .	49

6.1.	Piezoelectric Transducer Equivalent Model . . . . .	56
6.2.	Two-element Focused Array Geometry . . . . .	59
7.1.1.	Transducer Electrode Configuration . . . . .	63
7.2.1.	Voltage Amplifier Design . . . . .	65
7.2.2.	Acoustic Response of a Single Pulsed Ring . . . . .	66
7.2.3.	Block Diagram of Controller Electronics . . . . .	69
8.1.1.	Feedback Stabilized Michelson Interferometer . . . . .	73
8.1.2.	Optical Detection of the Reflected Acoustic Field . . . . .	74
A1.1.	Optical Fiber Cutter . . . . .	88
B2.1.	Strain Calibration Data . . . . .	91

Chapter I  
INTRODUCTION

The application of ultrasonic techniques to studies of material properties and nondestructive evaluation (NDE) of materials has experienced an explosive growth in the past 25 years. The key element in any ultrasonic system is the transducer which launches and/or detects the ultrasonic waves. The rapid growth in ultrasonic testing has resulted in the development and refinement of many transduction methods which include reversible techniques based on piezoelectric, electromagnetic, electrostatic, and magnetostrictive effects; mechanical and thermal sources of ultrasound; and mechanical, thermal, optical, and electrical detectors of ultrasound[1]. An ultrasonic evaluation system may include any one or a combination of the above techniques. The basic requirements of a good transducer as summarized by Sachse and Hsu[1] and listed below:

1. controlled frequency response,
2. absence of "ill" characteristics,
3. high power as a source,

4. high sensitivity as a receiver,
5. wide dynamic range,
6. linear electro-mechanical-acoustical response, and
7. controlled geometric radiation field effects.

Two ultrasonic evaluation systems have been investigated as part of this M. S. thesis research and are described here. The purpose of this research is to examine the two systems as possible means of materials evaluation without comparison as they are quite unrelated techniques. The first system is a non-contact receiving ultrasonic transducer system that utilizes an optical fiber interferometer as the receiving transducer. Specific applications in composite evaluation are suggested because of the similarity of the optical fiber to the matrix members in composites. Furthermore, this system provides a means of built-in evaluation that could be used from the initial manufacture of the composite to the end of the composite lifetime, and, because the optical fiber resembles graphite fiber, material integrity is not degraded by the addition of optical fibers. The second system is a pulse-echo ultrasonic transducer system that uses a piezoelectric transducer to generate a focused

bulk ultrasonic field for point probing and an interferometric optical system as the receiving transducer. The focused field from the transmitting transducer is electronically adjustable so the system can scan in three dimensions thus enabling tomographic reconstruction of the specimen under interrogation. This non-invasive technique of point probing has applications in materials characterization as well as biomedical engineering where it is desirable to examine tissue and organs for diagnostic purposes prior to treatment and/or operation.

The next four chapters discuss the first system while the last four chapters discuss the second system. The second chapter gives a brief history and overview of the development of optical fiber waveguides and their subsequent use as sensors. The third chapter details the theory of interferometry and analyzes the specific theory of an optical fiber Mach-Zehnder interferometer, the type used in the experiments discussed in the fourth chapter. The calibration of the interferometer is also discussed. Experimental details of the optical fiber interferometer are discussed in Chapter IV. In particular, a two-dimensional extension of the one-dimensional detection of strain is reported. The detection of acoustic emission in graphite epoxy composites

is also reported. Finally, a comparison of the use of single and multimode fiber, in the system in Chapter III is made. Chapter V summarizes the experimental results and compares the optical fiber interferometric system to existing evaluation methods.

The acoustooptical pulse-echo ultrasonic transducer system is discussed in Chapters VI-IX. Chapter VI gives some theoretical background and a brief summary of previous work in focusing transducers. Additionally, the three separate sub-systems in the overall transducer system are identified. The next two chapters discuss the sub-systems individually and identify some of the problems of total system integration. Chapter IX highlights the important aspects of the system, and some problems and limitations, and suggests further improvements to the system.

Finally, the appendices contain various experimental procedures that seem obvious in retrospect, but are actually a result of many problems encountered during the experimental phases of this work. They are intended as future reference as this research progresses in hopes that repetition of this work may be avoided.

## Chapter II

### OPTICAL FIBER BASICS

#### 2.1 OPTICAL FIBER DEVELOPMENT

The optical fiber waveguide was first developed for guided transmission of optical communications signals to avoid atmospheric disturbances. The practical importance of optical communications was not realized until the invention and development of lasers which produce a highly coherent light sources with large bandwidths suitable for signal transmission in the early 1960's[2]. Since 1966, when Kao and Hockham published the first paper on the use of optical fiber waveguide in optical communications systems, optical fibers have been applied to medical instrumentation, nondestructive testing, computer systems interconnection, process control and machine control systems, as well as military and civilian telecommunications[3-9].

#### 2.2 OPTICAL FIBER GEOMETRY

The types of dielectric waveguides used for guiding light waves are known as 'optical fibers' and are distinguished by the manner in which the index of refraction varies in the waveguide and by the number of modes which can propagate in

the fiber. The optical fiber waveguides may be categorized as follows:

1. multimode graded index: fiber index of refraction obeys the square law in the radial direction, and
2. single mode or multimode step index: fiber index of refraction changes abruptly as a function of radius defining regions of different but homogeneous refractive indices.

The fibers described above are called clad fibers. The cladding supports the inner glass core and prevents undesirable scattering and field distortion because the refractive indices of the inner ( $n_1$ ) and outer ( $n_2$ ) dielectric cylinders obey the relation[10]:

$$n_1 > n_2 \quad (2.2.1)$$

The clad fibers are made of silica-based glasses which are suitable for transmission in the near infrared wavelength range. Figure 2.2.1 shows the geometry of a typical optical fiber. The core and cladding are made from extremely high purity glasses in order to avoid impurity absorption losses. The outer layer can be made of the same material as the

cladding, but is generally less pure and therefore has a slightly different index of refraction than the cladding. The outer layer and protective coating increase the fiber diameter for easier handling and provide increased rigidity to resist bending[3]. The single mode fiber has a core diameter of 1-5  $\mu\text{m}$  which allows only the fundamental mode ( $\text{HE}_{11}$ ) to propagate in the fiber. This feature gives the single mode fiber the largest bandwidth of the three fiber types. The core of the multimode fiber is much larger (20-100  $\mu\text{m}$ ) and can either be of graded index or step index as in the single mode case. Because of the larger core diameter, more than one mode may propagate in the fiber; this lowers the bandwidth. Table 2.2.1 summarizes and compares the characteristics of the various fiber types. In addition to the glass fibers listed in Table 2.2.1, fibers with plastic cores and/or claddings have been developed[2].

Lightwave propagation is determined by reflection and interference assuming the light is contained in the fiber by total internal reflection within the core. An optical beam is transmitted into the core by inserting it at an angle  $\theta$  which must be larger than the critical angle for total internal reflection shown in Figure 2.2.1 and given by[2]:

$$\theta \geq \arcsin(n_2/n_1). \quad (2.2.2)$$

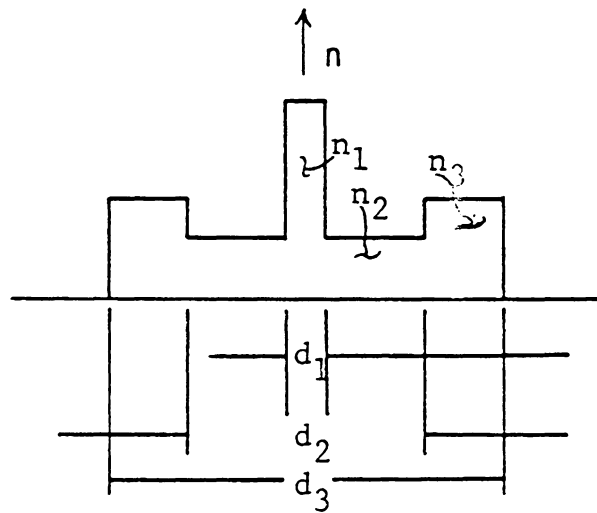
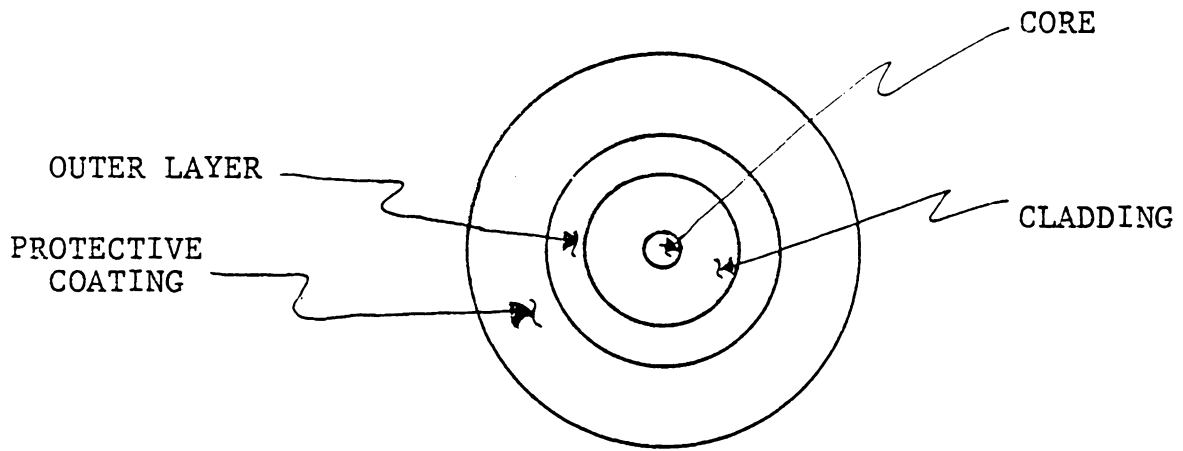


FIGURE 2.2.1: Single Mode Optical Fiber Geometry

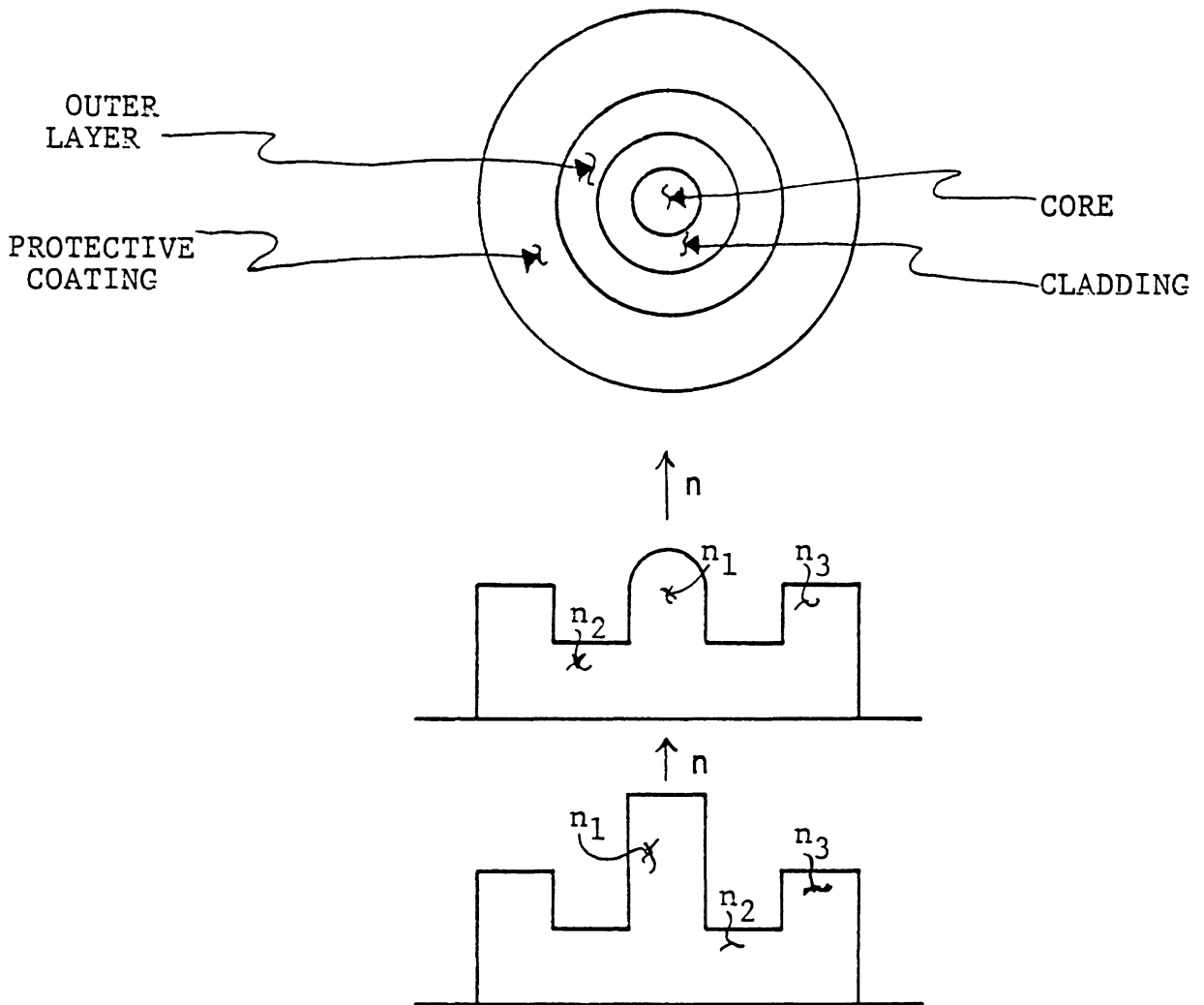


FIGURE 2.2.2: Multimode Optical Fiber Geometry

TABLE 2.2.1

## Types of Optical Fibers and Their Characteristics

FIBER TYPE	ATTENUATION	BANDWIDTH	CORE DIAMETER	CLADDING THICKNESS	
Single mode	~1dB/km (Scattering limit)	~40GHz-km (Material and waveguide dispersion)	$1\lambda-5\lambda$	$\geq 10$ times core size	10
Multimode graded index	~2dB/km (Scattering limit)	300MHz-km (Profile control, profile change with wavelength)	50-60 $\mu$ m	10 times core size	
Multimode step index	(Scattering or absorption limit)	20MHz-km (modal dispersion)	>80 $\mu$ m	$\geq 2$ times core size	

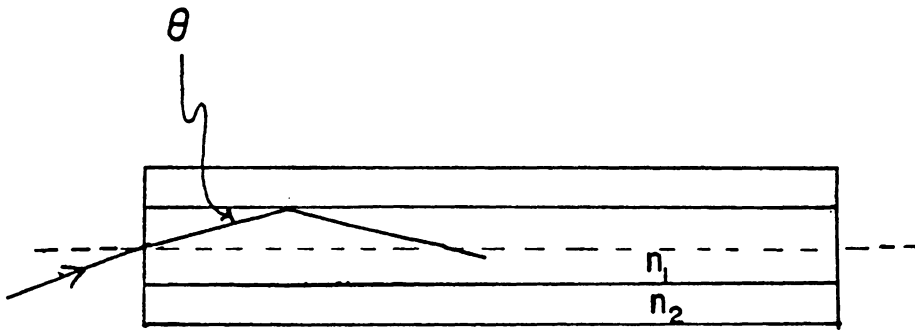


FIGURE 2.2.3: Optical Fiber Waveguide Ray Diagram

For constructive interference, the rays propagating in the core must superimpose themselves in a constructive manner which limits  $\theta$  further to a discrete set of values. While the geometry of a single mode fiber allows only the fundamental ( $HE_{1,1}$ ) mode to propagate in the core, multimode geometry allows any of the  $HE_{1m}$  modes to propagate in the core due to the increased core diameter[3]. The optical field at the output of the fiber may be expressed simply as

$$E = E_0 \exp[-j(\omega t - kx + \Delta\phi)], \quad (2.2.3)$$

where  $E_0$  is the maximum amplitude,  $k$  the propagation constant,  $\omega$  radian frequency, and  $\Delta\phi$  the phase shift due to the distance that the light propagates in the fiber. The phase  $\Delta\phi$  may be altered by dimensional and/or index of refraction changes in the fiber[6]. The sensitivity of the index of refraction to many physical phenomena makes the optical fiber an excellent sensor.

### 2.3 OPTICAL FIBER SENSORS

The first optical fiber sensor was developed by Vali and Shorthill[7] in 1976 for rotation rate sensing. Since that time sensors using optical fiber interferometers which are

phase sensitive have been applied directly by several authors to detect acoustic, magnetic, temperature, and pressure fields[4-10]. Primarily two types of single mode optical fiber sensor arrangements have been used in these applications. The first sensor is the single fiber sensor used by Vali and Shorthill[7] in rotation rate sensing. Figure 2.3.1 shows how the optical beam is sent into both ends of the loop. As the loop is rotated, the two beams see different optical phase shifts thus allowing the sensor to detect the rotation rate. The single fiber sensor is very susceptible to optical feedback[5] which induces an increased noise level in the laser from reflections back into the laser cavity. Additionally, the non-ideal characteristics of the single mode fiber may allow degenerate modes to propagate in the fiber. The relative balance between the degenerate modes is different for the counter rotating beams and can change as a function of position. This leads to severe environmental sensitivity and non-reciprocity.

A second and more desirable sensor arrangement is the Mach-Zehnder interferometer shown in Figure 2.3.2. The incident optical field from the laser is split by the beam-splitter; part of the beam is focused on the reference fiber (arm) and part is focused on the sample fiber (arm) which is

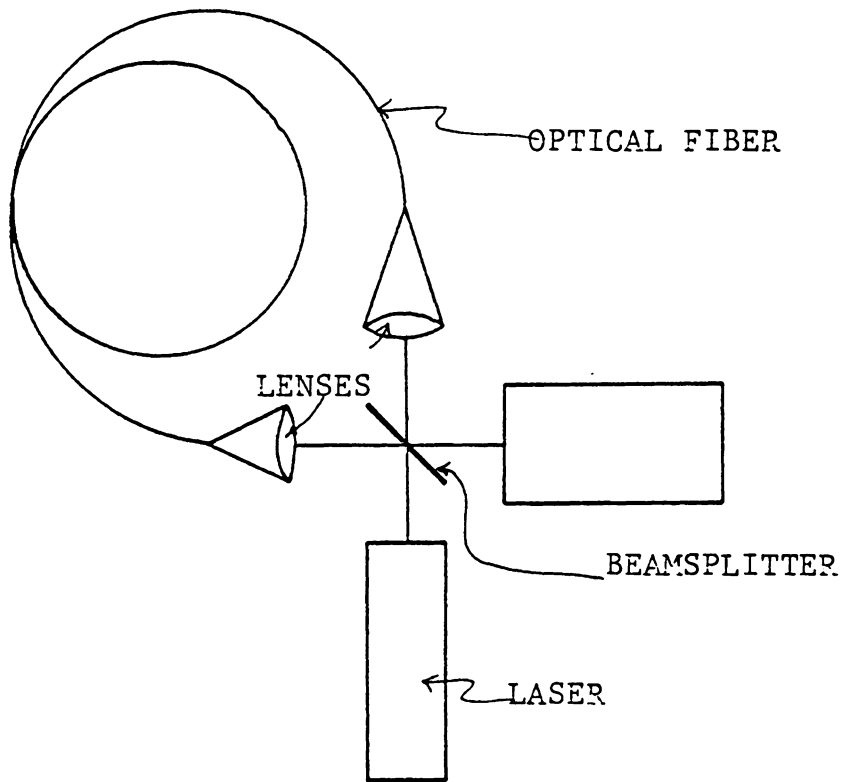


FIGURE 2.3.1: Single Fiber Optical Sensor

exposed to the field to be detected. The two beams are recombined at the output and allowed to interfere on the surface of an optical detector. As the field in the sample arm varies an optical phase shift is produced. The phase difference  $\Delta\phi$  induced in the interferometer is:

$$\Delta\phi = (2\pi/\lambda)2d \cos \theta, \quad (2.3.2)$$

where  $\lambda$  is the wavelength of the optical source,  $d$  the length of path interaction and  $\theta$  the angle of inclination of the light at the observation plane. Thus, the Mach-Zehnder interferometer is extremely sensitive because of the small wavelength of optical frequencies; furthermore, the sensitivity may be increased by lengthening the field interaction path[12]. Environmental noise may be reduced by maximizing the photoelastic coefficients of the core and by optimizing the elastomeric moduli of the protective jacketing on the fiber[5]. While the first optical fibers developed had substantial attenuation (30-50 dB/km) due to impurities in the glass, new techniques have been developed that yield optical fibers with attenuation which approaches the theoretical limit determined by Rayleigh scattering (1dB/km)[11]. Today the major limiting factor for the resolution in optical

fiber sensors is background noise introduced by the environment.

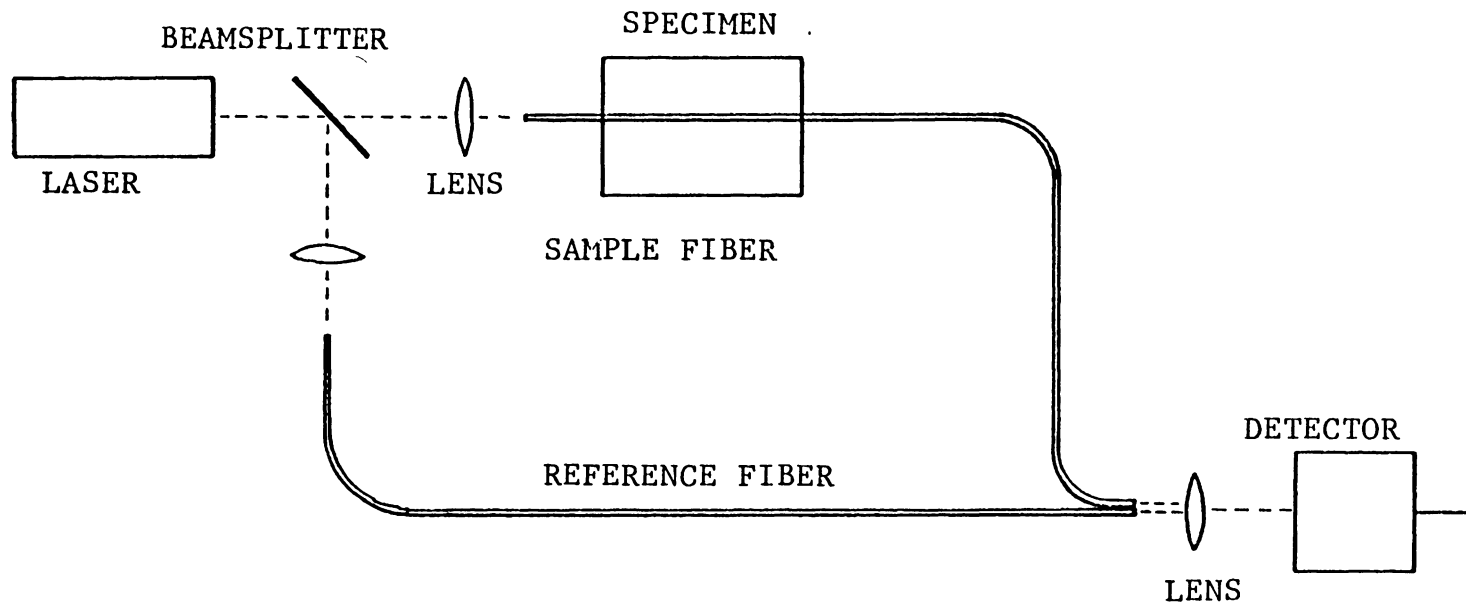


FIGURE 2.2.3: Mach-Zehnder Interferometer

## Chapter III

### OPTICAL FIBER INTERFEROMETRY

The modified Mach-Zehnder interferometer of Figure 2.3.2 is used to detect changes in the difference in the phase delay between two optical fiber paths. If the optical path-lengths are equal to within the coherence length of the source, optically heterodyning the light from the output of the two fibers produces a stationary pattern of dark and light interference fringes. The relative phase change of light from one fiber with respect to the other results in a displacement of the fringe pattern at the output. Spatial filtering of the light in the fringe pattern and optical detection of the transmitted light gives an electrical signal related to the pathlength difference  $\Delta L$  between the two fibers [3]. Although this relationship is a complicated nonlinear function in general, for small pathlengths  $\Delta L$  is directly proportional to the electrical output of the detector[6,14].

#### 3.1 FIBER INTERFEROMETER THEORY

Consider a fiber of length  $L$ , core diameter  $D$ , and core index of refraction  $n$ [6]. If the laser light has a free

space propagation constant  $k_0$ , and a single mode propagation constant  $k$  inside the fiber, then the relative retardation of the light that propagates through both fibers is

$$\phi_s = \phi_r = kL. \quad (3.1.1)$$

Deformation of the fiber due to an applied stress causes a phase shift at the output

$$\Delta\phi = \phi_s - \phi_r = k\Delta L + L\Delta k \quad (3.1.2)$$

for small applied stresses.

The first term in Equation 3.1.2 represents the optical phase modulation produced by a physical change in the length of the fiber due to strain. The second term is produced either by the strain-optic effect in the fiber material or by optical waveguide mode dispersion due to a change in fiber diameter. Thus the second term may be written as a sum of two terms

$$L(dk/dn)\Delta n + L(dk/dD)\Delta D. \quad (3.1.3)$$

Equation 3.1.2 then becomes:

$$\Delta\phi = PkL(2\nu-1)/E + L(dk/dn)\Delta n + L(k/D)\Delta D \quad (3.1.4)$$

where  $P$  is pressure,  $E$  Young's modulus and  $\nu$  Poisson's ratio [6,15]. Hocker [6] evaluated Equation 3.1.4 theoretically to determine the fiber sensitivity to pressure changes and found the sensitivity to static pressure changes to be low (154 kPa-m/fringe for a He-Ne laser source) compared to other methods. For an ITT-110 single mode optical fiber the phase shift per unit pressure per unit length is approximately

$$\Delta\phi/PL = 4.09 \times 10^{-5} \text{ rad/Pa-m.} \quad (3.1.1)$$

Additionally, there was a large uncertainty in measuring the pressure-induced fringe displacement because of the larger displacements caused by temperature variations [6].

### 3.2 OPTICAL SIGNAL DETECTION

The instantaneous amplitude of the light in the sample arm of the interferometer given in Equation 2.2.3 may be written as:

$$E = E_0 \exp j[\omega_0 t - k(x \sin \theta + z \cos \theta) + \phi], \quad (3.2.1)$$

where  $\phi$  is half the phase difference between the fields in the sample and reference arms and  $\theta$  the angle of incidence of the optical beam measured from a line normal to the surface of the detector. Similarly the instantaneous amplitude of the light in the reference arm is

$$E = E_0 \exp[j(\omega_0 t - k(x \sin \theta + z \cos \theta) + \phi)]. \quad (3.2.2)$$

The total instantaneous amplitude is the sum of the two fields in the region where the beams overlap so that the optical irradiance  $H = E \times E^*$  is then

$$H = 4E_0 \cos(kx \sin \theta + \phi) \quad (3.2.3)$$

which for small angles  $\theta$  becomes

$$H = 4E_0 \cos(kx\theta + \phi). \quad (3.2.4)$$

Equation 3.2.4 will be a maximum when

$$kx\theta + \phi = 0 \quad (3.2.5)$$

which implies the interference maxima occur at

$$x = (m\pi - \theta)/k\theta. \quad (3.2.6)$$

The changing phase of the beam results in a fringe shift in the  $x$  direction only. The amount of light transmitted by the Ronchi ruling as shown in Figure 4.1.1. will determine the amount of total modulation incident on the detector. For maximum modulation the Ronchi ruling must be placed so that the line spacing is equal to the fringe spacing:

$$\Delta x = d = \lambda/2\theta. \quad (3.2.7)$$

The transmitted light flux is then

$$\begin{aligned} \Phi &= m \int_{x_1}^{x_1 + \frac{\lambda}{2}} H(x) dx \\ &= m [E_0^2 d - (2E_0^2 d/\pi) \sin[(2\pi x_1/d) + (4\pi/\lambda)\Delta L]. \end{aligned} \quad (3.2.8)$$

Using the small signal approximation  $\Delta L \ll \lambda$  which is valid for the applied signals and neglecting the terms of the resulting expansion which are independent of optical path length change, Equation 3.2.8 becomes

$$\Phi = m [E_0^2 d - E_0^2 d (8\Delta L/\lambda)]. \quad (3.2.9)$$

Equation 3.2.9 shows that the total signal is composed of a dc light flux incident on the detector and a light flux which depends on the phase shift. The dc term is the major source of shot noise in the detector. If the laser has a total incident power  $P_0$ , then the incident power transmitted to the detector is given by:

$$P = (P_0/2) - P_0(4\Delta L/\lambda). \quad (3.2.10)$$

Because the Ronchi ruling transmits only half the power the detector receives  $P_0/2 \propto mE_0^2d$ . The signal current at the output of the detector is proportional to the incident power and is given by

$$i_s = 4\alpha P_0 \Delta\phi / 2\lambda \quad (3.2.11)$$

where  $\alpha$  is the sensitivity of the optical detector[15,16]. The output signal current may be processed to obtain information about the acoustic signal.

### 3.3 CALIBRATION

The fiber interferometric system has been calibrated using a cantilever beam geometry in a differential system as

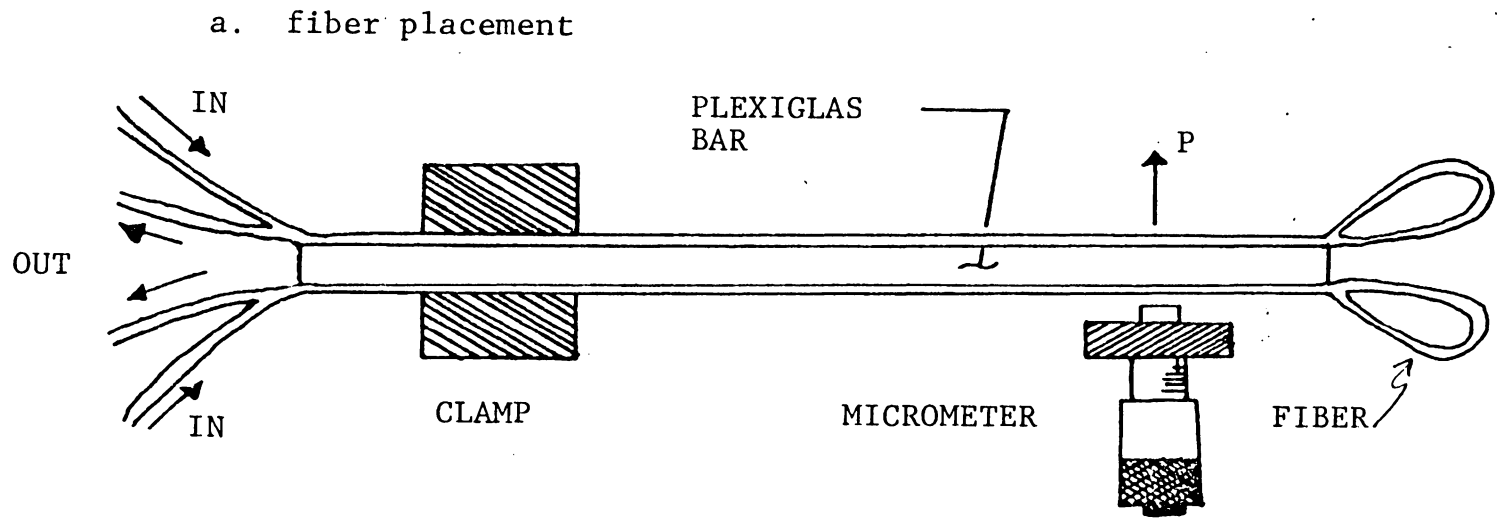
shown in Figure 3.3.1 where the single mode fibers are adhesively bonded to both sides of a plexiglass bar[12]. Additionally, the two fibers are doubled on each side of the 0.32 cm thick 15 cm long bar to increase the sensitivity of the system. As a pressure  $p$  is applied at the unclamped end by the micrometer, one fiber is in tension while the other fiber is in compression, thus the fringe shift at the output is proportional to twice the strain in the bar. For the geometry in Figure 3.3.1, the strain is given by[16]:

$$\epsilon = 3da/4L^2 \quad (3.3.1)$$

and

$$\Delta\phi \propto \Delta\epsilon = 2\epsilon. \quad (3.3.2)$$

The dc strain sensitivity calibration data is shown in Figure 3.3.2 as a function of bar length. The average experimental error was 8%. Calibration data and calculations are given in Appendix B.



b. geometry

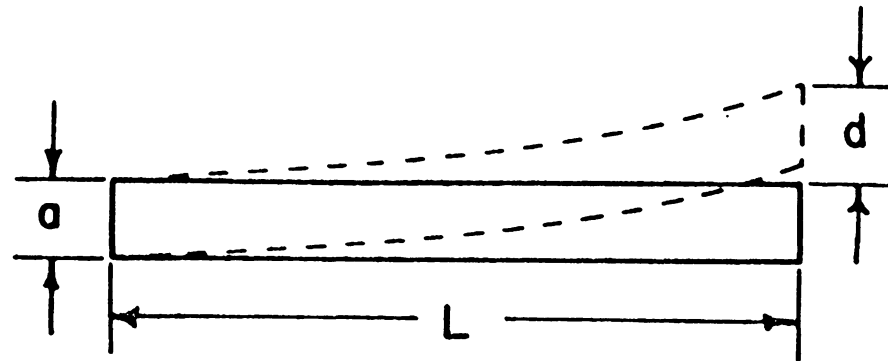


FIGURE 3.3.1: Cantilever Beam Calibration Experiment

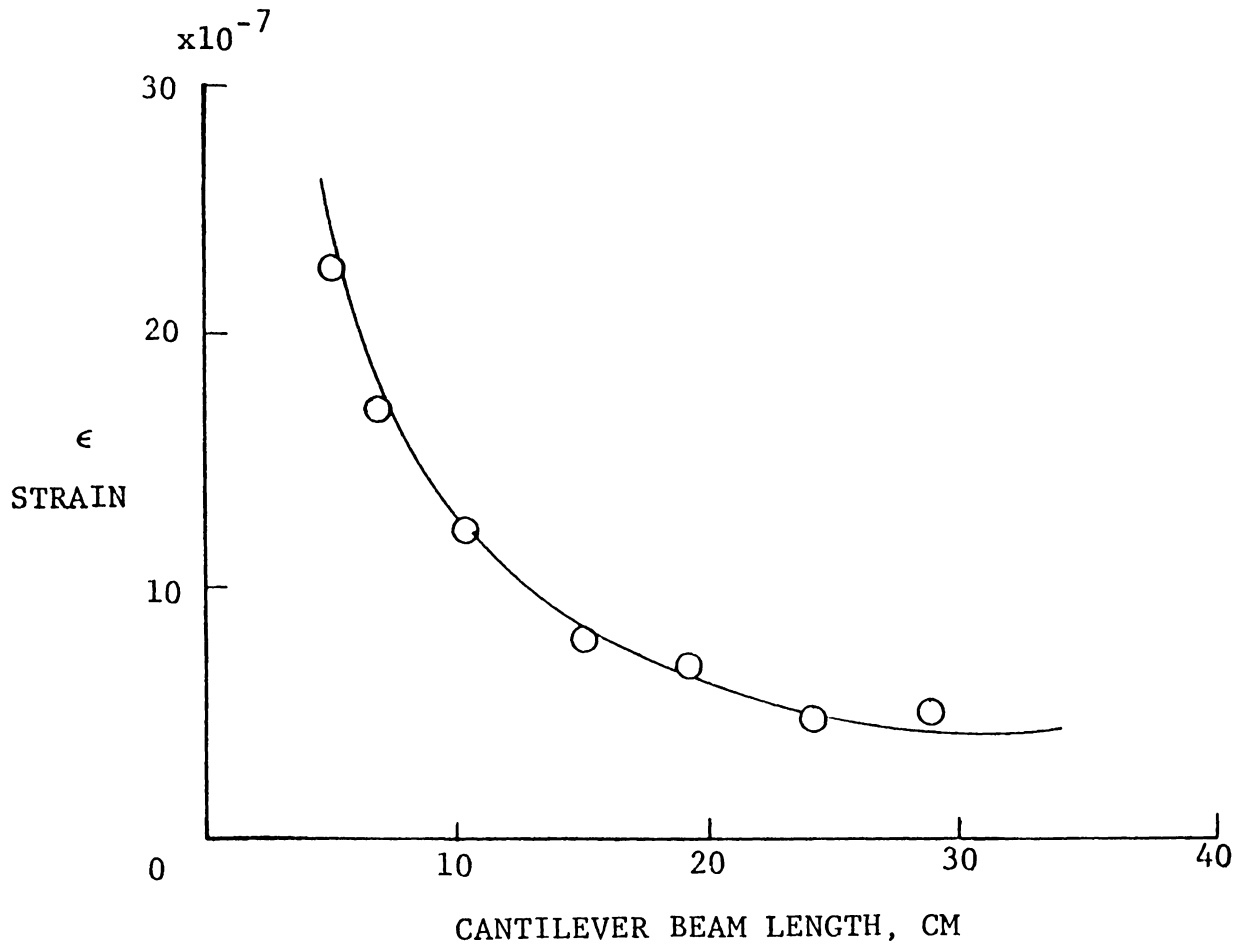


FIGURE 3.3.2: Calibration Curve

## Chapter IV

### EXPERIMENT

An optical fiber interferometric system was constructed as shown in Figure 4.1.1. An adaptively stabilized 0.5 mW helium-neon laser source was collimated, expanded, divided into two beams by the beamsplitter, and focused using 10x microscope objectives onto the input ends of two ITT-110 single mode fibers. The external plastic jacketing and inner RTV sleeving were removed from the first centimeters of the 4.5  $\mu\text{m}$  core diameter fibers, and approximately 4 cm of the exposed fiber was painted with index matching mode stripping fluid. Several sample fibers were prepared and then attached to various materials. The purpose of the experiment was three-fold:

1. to extend the one-dimensional strain calibration to two dimensions,
2. to detect acoustic emission events using optical fiber sensors, and
3. to examine some qualitative NDE techniques using multimode optical fibers.

#### 4.1 OPTICAL DETECTION OF STRAIN IN TWO-DIMENSIONS

A 15.24 cm x 15.24 cm rectangular plate was cut from a plexiglass sheet 0.32 cm thick. Six single mode optical fibers nominally 0.5 m long were attached to the plate as shown in Figure 4.1.2. The plate was simply supported at each corner and a point source displacement was applied at each location indicated by the labeled circles in Figure 4.1.2. As in the cantilever beam calibration experiment, the displacement compresses the attached fibers causing an incremental change in the fiber length. If one fiber is used as the sample arm of the interferometer in Figure 4.1.1, the compression causes a phase shift in the output of the interferometer. By sampling each fiber of the matrix, the normal strain throughout the plate may be determined. At each circle on the plate, a 0.04 cm displacement was applied and the output response of each fiber was recorded on an x-y plotter connected to the output of the optical detector. Examination of each individual fiber for the same displacement yielded a two-dimensional matrix of the dc strain in the plate.

The equation governing the deflection of a plate is given by:

$$\nabla^4 w = 12(1-\nu^2)P/Et^3 \quad (4.1.1)$$

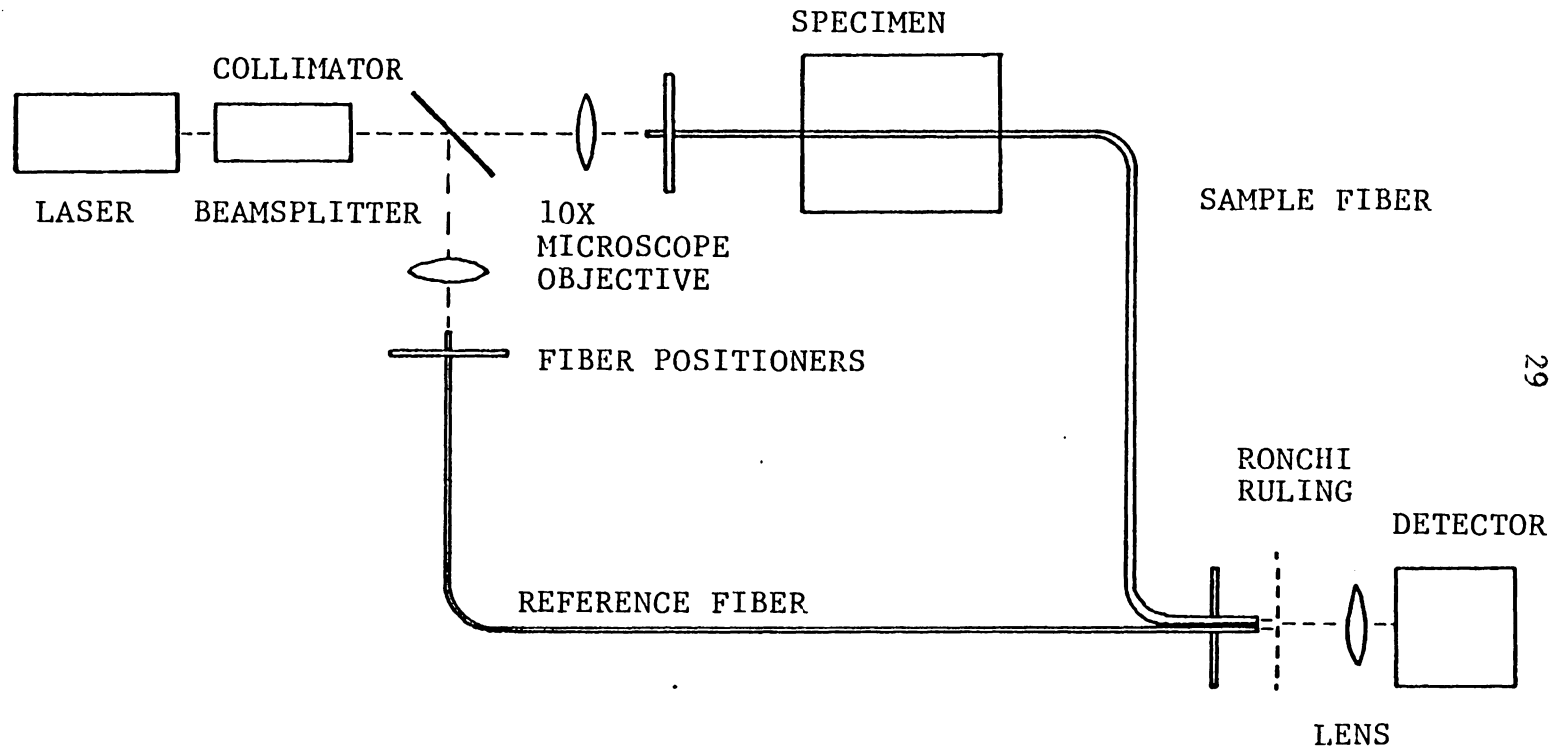


FIGURE 4.1.1: Optical Fiber Interferometric System

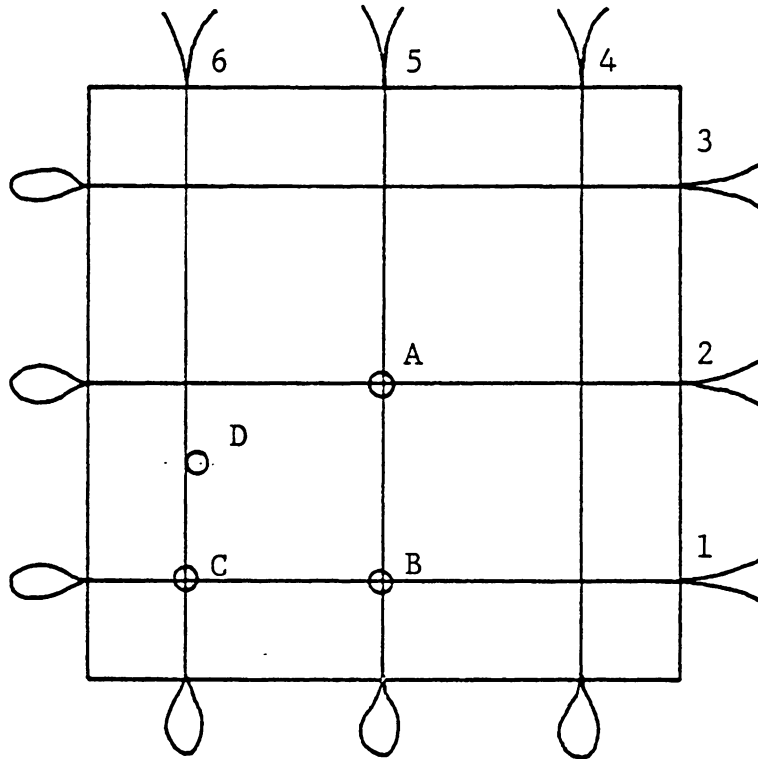


FIGURE 4.1.2:  
Rectangular Plate with Fiber Matrix Attached

where  $w$  is displacement,  $E$  Young's modulus,  $t$  thickness, and  $\nu$  Poisson's ratio. Once the displacement is known at each node, the normal strains  $\epsilon_x$  and  $\epsilon_y$  may be calculated using [17]:

$$\epsilon_x = -z \partial^2 w / \partial x^2 \quad (4.1.2 \text{ a})$$

$$\epsilon_y = -z \partial^2 w / \partial y^2. \quad (4.1.2 \text{ b})$$

The solutions for equations 4.1.1 and 4.1.2 for a corner-supported plate are best obtained using a finite element approach with the proper boundary conditions for each node in the analysis[17,18]. For the applied stress at 'A,' the strain over the entire plate was calculated using a quarter plate section and the properties of symmetry were applied to obtain a total solution. By sectioning the quarter plate as shown in Figure 4.1.3, nodes 1-5 lie along fiber 2 in Figure 4.1.1. Similarly, nodes 16-20 lie along fiber 3, nodes 3, 7, 11, 15, and 24 along fiber 4, and 1, 6, 11, 16, and 21 along fiber 5. By symmetry, the stress along fiber 1 is the same as that along fiber 3 and fiber 6 is the same as that along fiber 4. The average strain was calculated by multiplying the incremental length of each section by the strain

for the node corresponding to that section. For example, the strain along fiber 2 is given by:

$$\varepsilon_x = 4(1.27\varepsilon_1 + 2.54\varepsilon_2 + 1.91\varepsilon_3 + 1.27\varepsilon_4), \quad (4.1.3)$$

where the factor of 4 arises due to the double length of the fiber and the quarter plate symmetry. The number of shifted fringes is then:

$$N = \varepsilon / \lambda. \quad (4.1.4)$$

For the asymmetrical loading of points B-D, the entire plate must be used in the analysis to obtain the correct solution. The experimental values are compared to the theoretical values for the symmetric case of the load at 'A' in Table 4.1.1.

The large discrepancies in the experimental and theoretical data are the result of several factors. The first problem arises in the theoretical modeling of a physically simple problem. The point-supported corners create singularities for boundary conditions which cause the solution about these points to be undefined. Because the boundary conditions are singular, a closed form solution cannot be

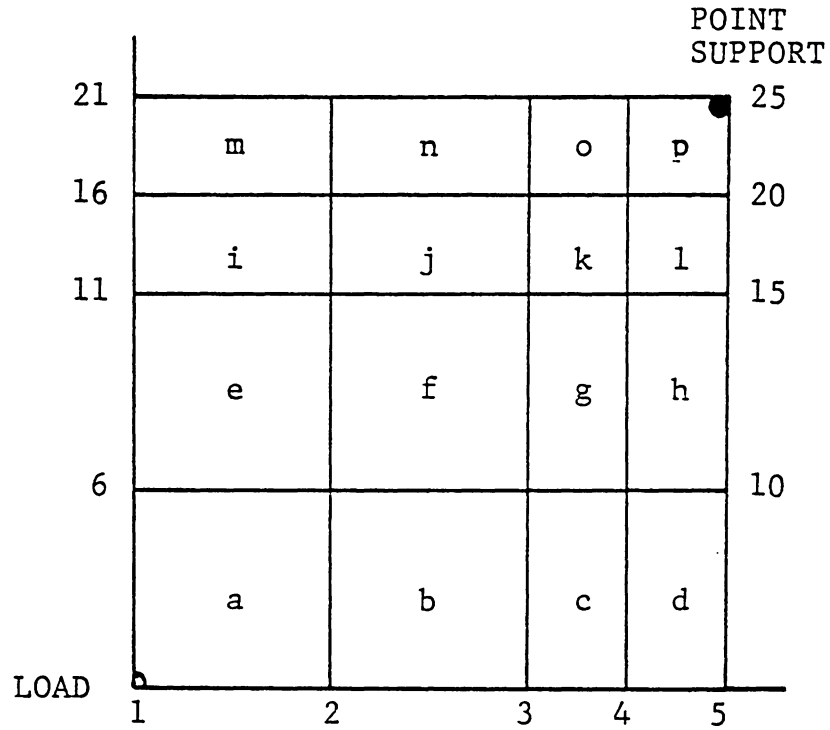


FIGURE 4.1.3:  
Partitions Used in the Finite Element Analysis Program

TABLE 4.1.1

## Theoretical and Experimental Strain Data

FIBER NUMBER	THEORETICAL NUMBER OF FRINGES	EXPERIMENTAL NUMBER OF FRINGES
1	99.5	37.5
2	48.4	22.0
3	99.5	39.0
4	99.5	31.0
5	23.3	24.3
6	99.5	30.5

obtained so a finite element analysis approach is required. Finite element analysis yields useful solutions in the analysis of plates and shells but still does not give accurate results near the singular conditions. The accuracy may be improved by using smaller sections near the singularities; however this requires much more computer storage for the nodal matrices as well as extended computing time which becomes prohibitive. Additionally, the finite element analysis is a pointwise approximation to a continuous phenomenon, in this case strain. The solutions from this analysis are the normal strains in the x and y directions at the center of each section; but the experimental data was the integrated strain along the fiber length attached to the plate. To obtain values for comparison, the values obtained from the computer solution were multiplied by incremental lengths according to the section size as shown in Figure 4.1.2 and noted in Equation 4.1.3. This method of modeling assumes a linear variation in strain which is a first order approximation.

Finally, there are two mechanisms modulating the fiber as discussed in Chapter III, namely, the strain in the direction normal to the fiber axis which changes the length of the fiber and the strain parallel to the lateral surface

of the fiber causing a change in the fiber diameter. As in the cantilever beam case the change in diameter was assumed small compared to the change in length and was neglected. For the two-dimensional case, the diameter change may be the same order of magnitude as the modulation due to pathlength change because of the two-dimensional nature of the applied load. This suggests a need for a more accurate mathematical model as well as a more complex data acquisition scheme that would yield vector component information about the strain on the fiber. The results in Table 4.1.1 are not entirely useless, however, because they indicate the optical fiber matrix is detecting the symmetries of the strain in the plate due to the applied load at A; that is, fibers 3 and 1 have similar outputs as do fibers 4 and 6. Additionally, fibers 2 and 5 have fewer fringe displacements than fibers 1, 3, 4, and 6 as expected from the theoretical analysis. The experiment has given a qualitative picture of the strain in the plate.

#### 4.2 ACOUSTIC EMISSION

An acoustic emission event is a pulsed ultrasonic wave generated internally in a material during a dynamic process. The frequency of an acoustic emission event varies depending

on the material and the nature of the dynamic process which caused it; however, many authors confine the frequency range of acoustic emission between 10 kHz and 1 MHz[19,20]. If an optical fiber were embedded in a material, the stress wave generated by the acoustic emission event would modulate the light transmitted through the optical fiber waveguide. By decomposing the acoustic field into vector components perpendicular and parallel to the axial direction of the fiber, the mechanisms of modulation may be defined. The acoustic wave generated parallel to the axial direction of the fiber will compress the fiber thus altering  $n$  and  $k$ , while the acoustic wave component perpendicular to the axial direction of the fiber alters the length of the fiber[6,20,21]. In general, the stress waves generated by an acoustic emission event occur at an angle that is arbitrary with respect to the fiber axis and the induced optical modulation is therefore a combination of the two effects. A remote event creates an uneven pressure distribution along the fiber that is spatially dependent on the angle measured along a radial line from the source to the fiber. The angular dependence has been analyzed for a remote linear source and was found to produce the same acoustic pressure on the surface of the fiber at the azimuthal angle as an identical source having

the same velocity and located at the surface of the fiber at the same angle[20,21]. The output of the embedded fiber is effectively the integrated strain along the embedded fiber length so the pressure analysis in Chapter III is assumed valid.

The mechanical resemblance of an optical fiber to the fiber members of a composite matrix indicates that replacing some of the composite fibers with optical fibers may provide a viable method for sampling acoustic emission events as well as internal residual stress fields. Also, this will not degrade the mechanical strength of the composite. The responses of single mode and multimode fibers as acoustic sensors were examined in graphite epoxy composites, SMC short chopped fiber composites, and casting plastic using the optical system discussed previously. Figure 4.2.1 shows the experimental configuration used to compare the fiber response with the response of a standard piezoelectric transducer. The prestressed graphite epoxy specimen was clamped at one end and a pressure was applied to the unclamped end. The fiber was adhesively bonded perpendicular to the direction of the top composite fiber matrix layer a few centimeters away from the clamp to eliminate dc strain effects due to bending. As the external pressure was applied, internal

stress fields were generated which resulted in matrix separation, layer delamination, or fiber breakage, all of which induced acoustic emission events. Figure 4.2.2a shows the fiber embedded in casting plastic while Figure 4.2.2b shows the optical fiber in an additional protective plastic sleeve and molded into an SMC short chopped fiber block. Figures 4.2.3a and 4.2.3b show typical acoustic emission events as detected by the optical fiber and the piezoelectric transducer, respectively. The optical fiber in each of the three geometries was placed with the reference fiber in a three-axis fiber mount so that the emerging beams were recombined to produce straight line interference patterns. The intensity pattern was spatially filtered using a Ronchi ruling. The resulting center circular fringe at the output of the Ronchi ruling was filtered using an iris and focused on the input of an optical detector.

The output of the optical detector was used in two different data acquisition systems. The acoustic emission events in Figures 4.2.3a and 4.2.3b were recorded on a Tektronix 7001 digitizing oscilloscope and then processed using a PDP11-34 minicomputer to obtain the frequency responses of Figures 4.2.4a and 4.2.4b. The calibration data as well as the data from the rectangular plate were obtained using a

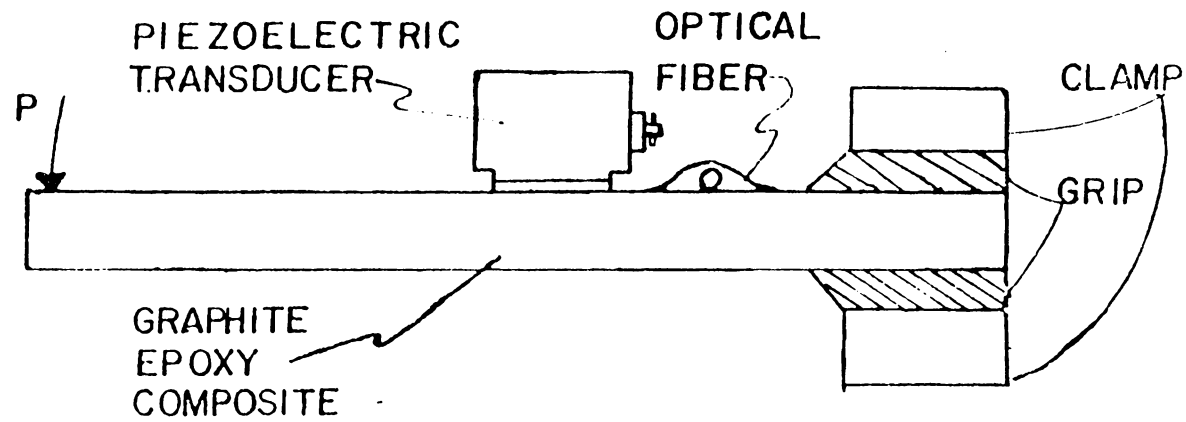


FIGURE 4.2.1; Experimental Configuration for Acoustic Emission Detection Comparison

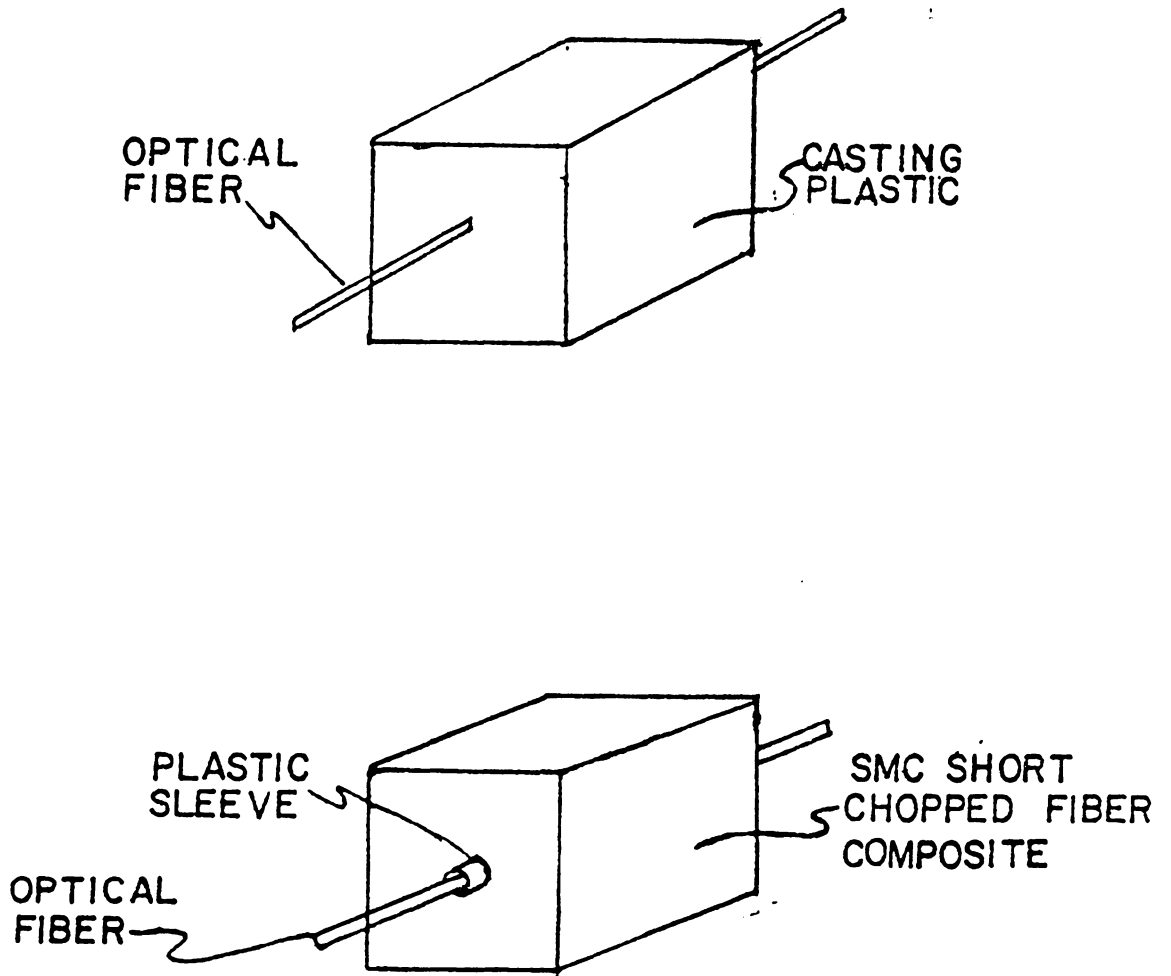
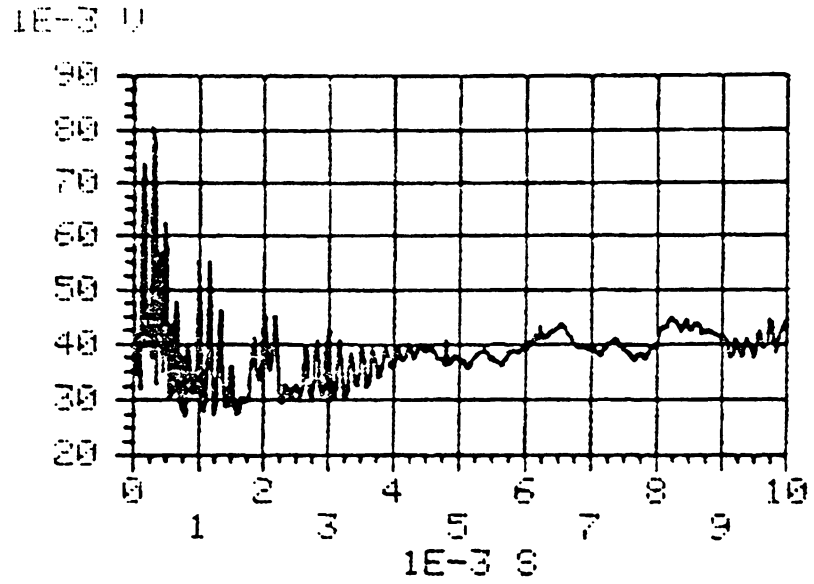
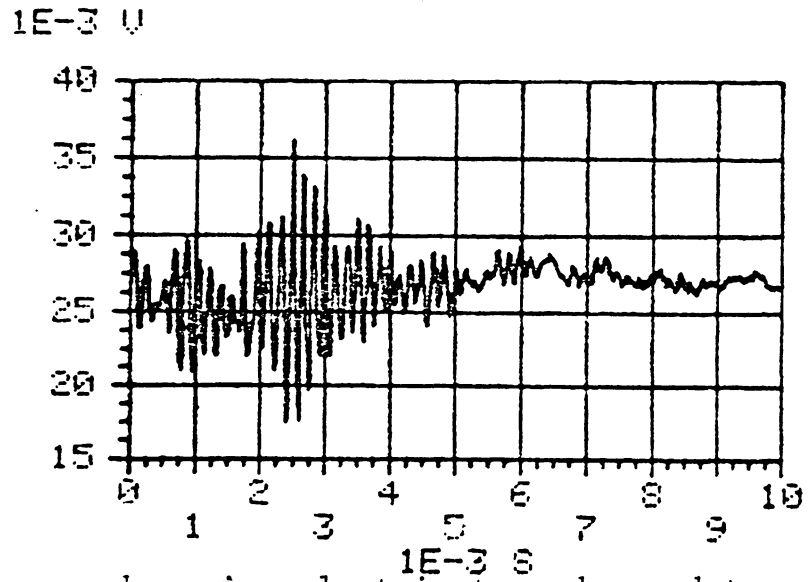


FIGURE 4.2.2: Embedded Optical Fibers in other Materials

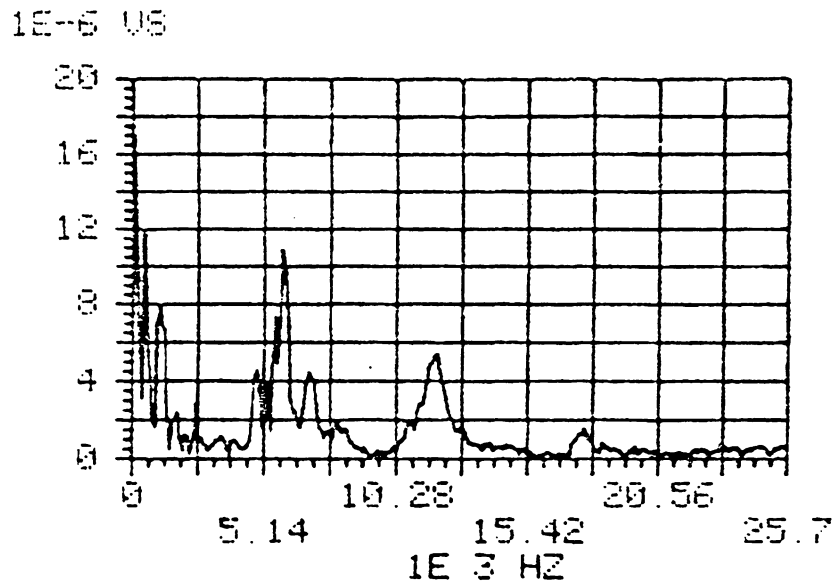


a. optical fiber data

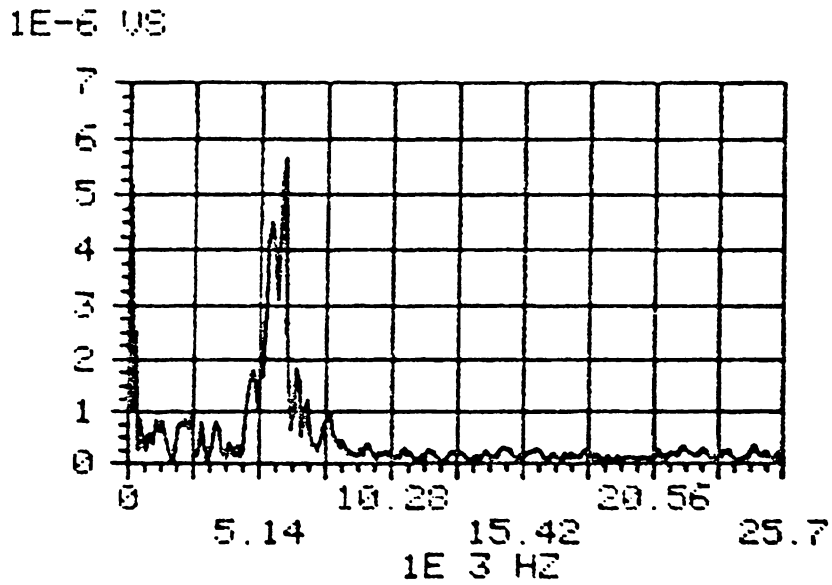


b. piezoelectric transducer data

FIGURE 4.2.3: Acoustic Emission Event:  
Time Domain Response



a. optical fiber data



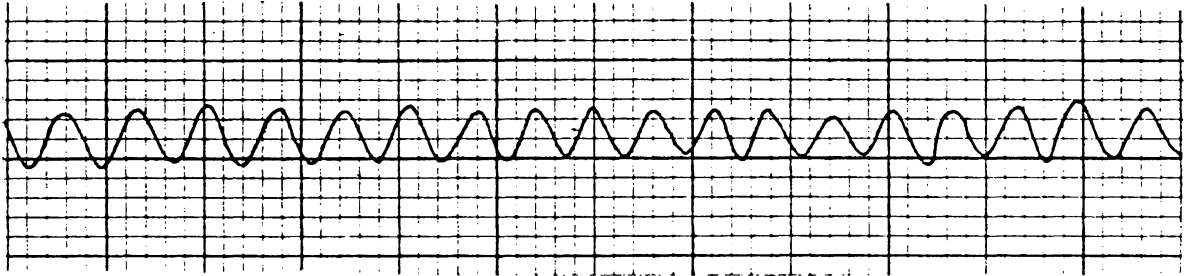
b. piezoelectric transducer data

FIGURE 4.2.4: Acoustic Emission Event:  
Frequency Domain Response

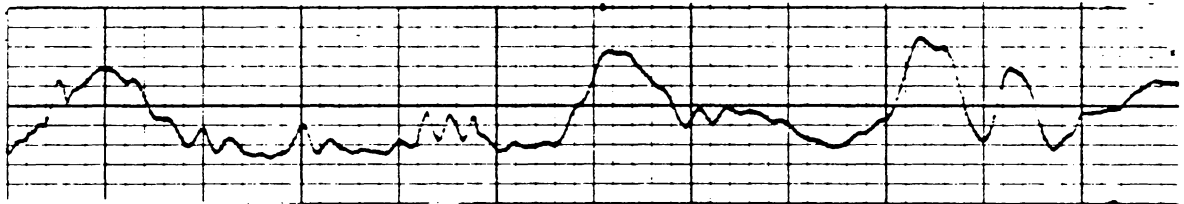
Houston Instruments x-y plotter. The x-y plotter was also used to compare the response of single mode and multimode fibers in the Mach-Zehnder interferometer. A multimode fiber was glued to the cantilever beam discussed in Chapter III and a load force was applied to the unclamped end of the bar. Figure 4.2.5a and 4.2.5b compare the single mode and multimode responses and indicate that the multimode fiber is an unsuitable sensor using this type of an interferometer. Other more complicated filtering techniques could be employed to obtain data from a multimode system.

#### 4.3 APPLICATION OF MULTIMODE FIBER IN NDE

The use of multimode optical fibers for the qualitative nondestructive evaluation of mechanical structures has also been reported by several authors. Specifically, two-dimensional grids of multimode fiber have been adhesively bonded to the surface of the European commercial jetliner Airbus[4] as well as embedded inside fiber reinforced plastic composites[22,23]. In this application, light transmitted through the array of perpendicularly oriented sample fibers is continuously monitored. If the host specimen undergoes excessive localized stress due to fatigue or impact, the fibers in the vicinity of the high mechanical load will



a. single mode fiber data



b. multimode fiber data

FIGURE 4.2.5: Comparison of Single Mode and Multimode Optical Fiber Data

break. By noting the pattern of transmitting and non-transmitting fibers, the location of the load may be determined and other NDE techniques employed for further quantitative inspection.

One advantage of this type of NDE system is overall simplicity. Since the absolute intensity of transmitted light is not important, alignment is not critical and inexpensive multimode glass or plastic fibers having relatively high losses may be used. Additionally, amplitude modulation caused by external temperature or stress gradients do not alter system measurements as they do in interferometric systems. Finally, detection and fault location may be performed by simple logic circuitry.

Despite the simplicity of this system, it has several serious limitations. First, the observable data are qualitative; only localized mechanical loads which result in fiber breakage can be detected. Second, once a fiber is broken inside the specimen it cannot be repaired so continued stress monitoring is not possible. Third, and perhaps most important, the mechanism of fiber breakage and the occurrence of defects related to failure has not been established[4].

To demonstrate the potential of this type of technique a simple experiment was performed. Multimode Corning glass fibers nominally one meter in length were glued between two 15.24 cm x 15.24 cm sheets of thin plastic as shown in Figure 4.3.1. Incoherent light was transmitted through each of the fibers to verify fiber continuity prior to applying a mechanical load. The load was applied as shown in Figure 4.3.2 by dropping a 0.62 kg weight 1.0 m to produce an approximation to a space and time delta function load at the center of the plastic sheets supported between two aluminum plates. As indicated, both fibers near the point of maximum load were broken, thus demonstrating quantitatively that fiber breakage can indicate load location.

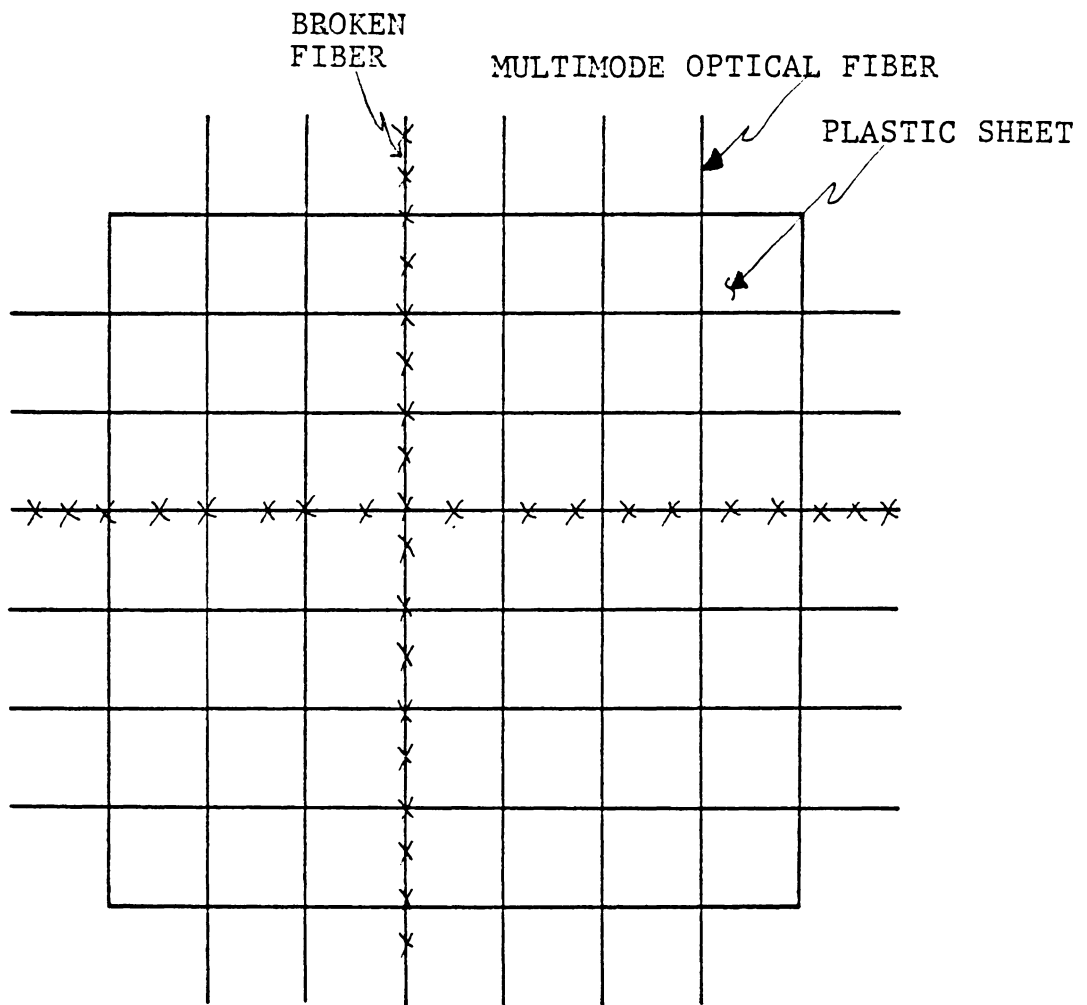


FIGURE 4.3.1: Laminated Plastic Sheet with Embedded Multimode Fibers

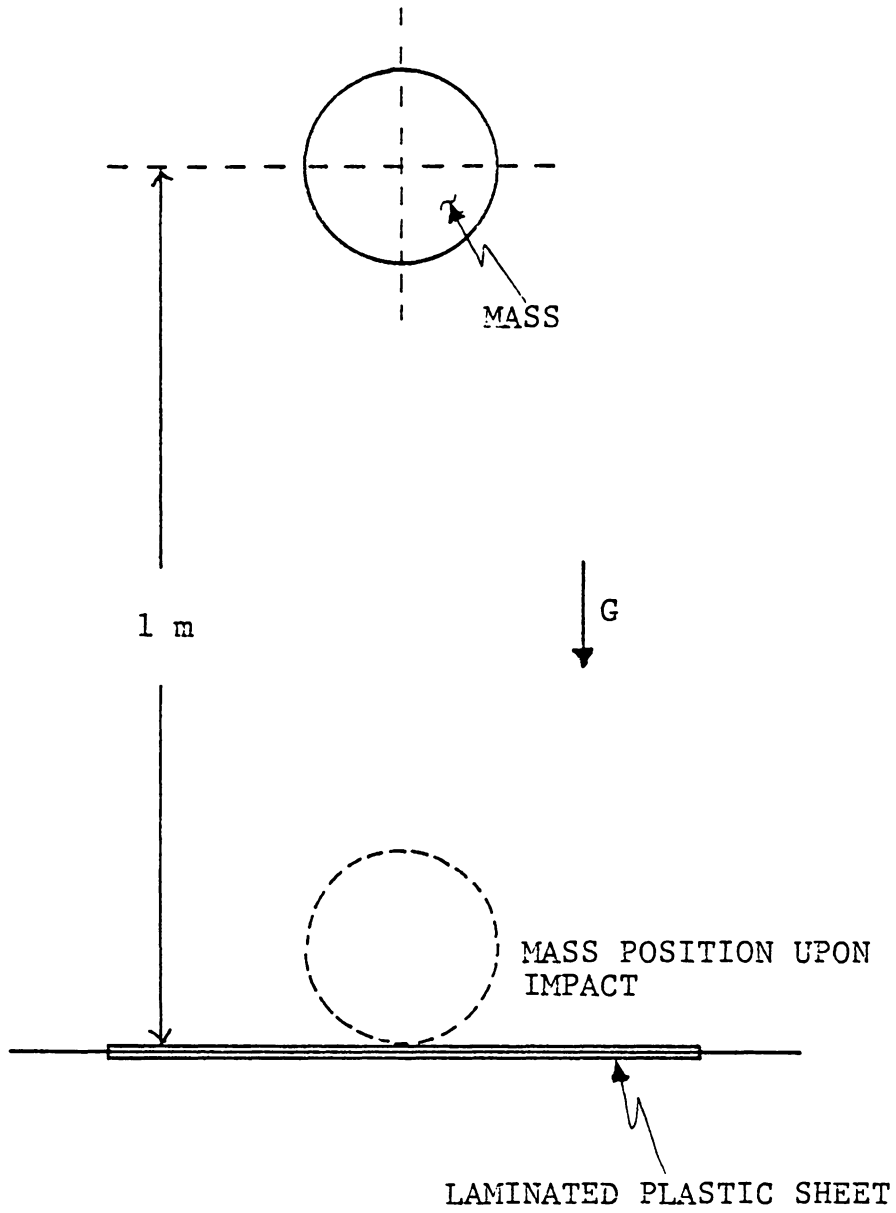


FIGURE 4.3.2: Position of Load Prior to Release

## Chapter V

### OPTICAL FIBER INTERFEROMETRY CONCLUSIONS

The modified Mach-Zehnder optical fiber interferometer is an excellent acoustic sensor because its sensitivity is limited only by the wavelength of the optical source. Embedding optical fibers in composites at the time of manufacture provides a built-in method of indirectly sampling internal stress fields during the life of the material. This non-contact method of sensing can be used to directly detect slowly varying residual stresses as well as pulsed acoustic emission events because of the broadband characteristics of the single mode optical fiber. By spacing the embedded fibers in each layer of the composite matrix and scanning the fibers in order, a three-dimensional reconstruction of the internal stress fields may be obtained. The detection capability of the optical fiber matrix makes it a potentially useful tool in nondestructive testing and materials evaluation. The fiber bandwidth response is limited by the coupling characteristics of the fiber-resin boundary between the fiber and composite. The jacketing around the fiber will also influence the performance of the fiber. In addition the mechanical properties of the jacketing may be optimized to increase the overall fiber sensitivity.

The experimental calibration data agree within 8% of the predicted theoretical data and also indicate an improvement in the minimum detectable strain to approximately  $10^{-10}$  using spatial filtering [15,16]; however, the extreme sensitivity to temperature and other environmental noise degrades the performance of the interferometer as an acoustic monitor. The environmental problems such as disturbances in the air from movement or talking create false interference patterns and often perturb the output of the interferometer so severely that the fibers become misaligned. Alignment of the optical fields emitted from the 5  $\mu\text{m}$  diameter ends of two fibers is critical and often requires hours of adjustment before an output suitable for detection is obtained. Presently there is no method of automatic adjustment to help eliminate this problem.

Before this optical fiber interferometric system could be implemented in an industrial environment, simple repeatable methods for cutting the fibers to achieve a flat surface perpendicular to the fiber axis must be developed. Additionally, the alignment process requires refinement and automation. A possible solution to this problem may lie in motor driven fiber mounts controlled by a microprocessor system that could first adjust the mounts so that the output

fields of the fiber coincided, and then maintain the interference pattern. Computer control of the alignment process could simplify the data acquisition so that a test procedure could be developed and implemented easily. Finally the ends of the embedded fibers require protection to prevent breaking or chipping that would distort the field to be detected and thus destroy the ability of the fiber system to act as an acoustic sensor.

The problems encountered during this research emphasize several points to be considered in any research. While experimental results unbiased by prior theoretical solutions are desirable, simple physical problems are not always simple mathematical problems. Therefore, detailed theoretical analysis should be outlined prior to experimentation so that the initial experimental conditions may be chosen to obtain a solution that is mathematically and physically meaningful. Practical considerations such as modeling and implementation of the proposed project should be reviewed and the resulting problems should be addressed. For example, the ability of the optical fiber interferometer to act as an acoustic monitor has been demonstrated but demonstration of an acoustic monitor has also emphasized the lack of knowledge in the modeling certain physical problems as well as the need for a

more comprehensive understanding of flaw characterization. The completion of the defined goals has created additional areas of research in materials characterization and in the practical problems of implementation of the fiber interferometric system.

## Chapter VI

### PIEZOELECTRIC TRANSDUCERS IN PULSED ULTRASONIC SYSTEMS

One of the most common reversible ultrasonic transducers used today is the piezoelectric transducer. The word 'piezo' is derived from the Greek word meaning 'to press;' thus, piezoelectricity is pressure electricity[24]. The piezoelectric effect occurs only in insulating solids with no center of symmetry because it is effectively the result of an induced dipole moment in the crystal due to the coupling between the elastic and piezoelectric constants. The dipole moment induced by an applied electric field results in a net strain produced by a shortening of bonds in the crystal in a direction parallel to the applied field. The piezoelectric effect is found in many crystals; however, quartz is the most frequently used material because of its stability, durability, and low cost. While there are many theoretical models for piezoelectric transducer elements, one of the most useful descriptions of the generation of bulk longitudinal waves may be obtained using the three-port electrical network described by Mason[1]. This network, shown in Figure 6.1, provides a one-dimensional model of the piezoelectric coupling between the acoustic and electromag-

netic fields which is applicable to the x-cut quartz crystal used in the experiment to be described. In addition, Figure 6.1 illustrates the reciprocity of the transducer which indicates that it may be used either as a transmitter or a receiver. The piezoelectric plate is modeled as an electrical transmission line which resonates at an operating frequency corresponding to the damped mechanical natural frequency of the crystal[1]. Thus, the transmitted ultrasonic field is then controlled by the applied voltage distribution on the crystal.

A transducer output beam may be shaped by varying the shape of the material, the piezoelectric constant, the electrode shape and/or spacing, or by using external lenses or reflectors to shape the beam after it has been launched from the transducer[1,24]. Focused piezoelectric transducers have been implemented using profiled transducer surfaces, various electrode shapes and spacings, as well as lenses. Another method of focusing an ultrasonic beam incorporates an array of transducer elements pulsed in such a way that the resulting fields from the elements add for field maxima and effective focus in space. Because of widespread applications in electromagnetics and acoustics, array theory is well-developed for the steady state or cw case. The high

$Z_o$ =mechanical impedance     $C_o$ =zero strain capacitance  
 $k$ =wave number

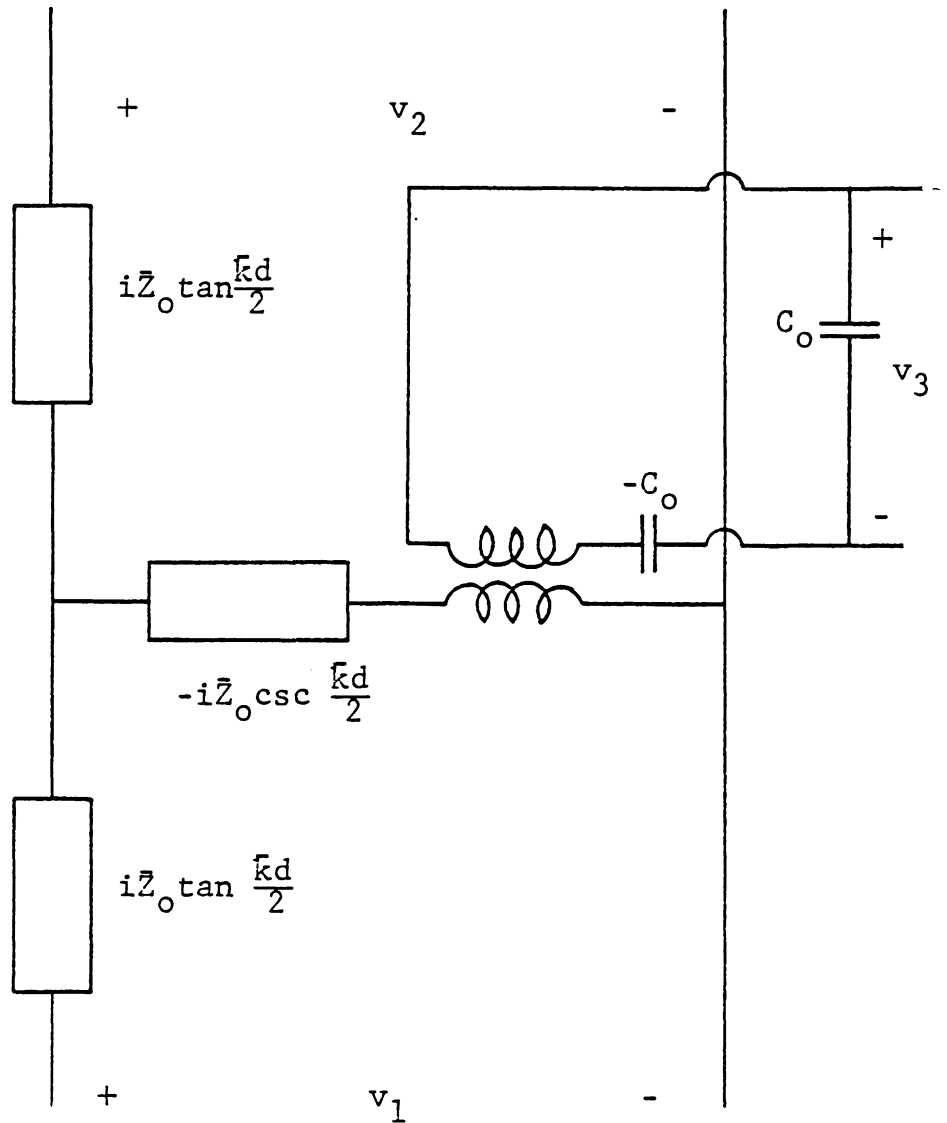


FIGURE 6.1: Piezoelectric Transducer Equivalent Circuit [25]

velocity of propagation of electromagnetic waves makes even a short time duration electromagnetic pulse physically long in space. Hence, the cw analysis is sufficient in electromagnetics; however, in ultrasonic pulse-echo systems, the short time pulse is spatially short also because of the slow velocity of propagation. The physically short pulse is both a common and necessary occurrence in ultrasonic materials characterization; therefore a theory for pulsed fields must be examined. Stephanishen and others[26-30] have investigated the transient response of piston radiators and found that the radiation patterns varied considerably from those obtained from steady state solutions, particularly in the near field where the nulls vanished as a function of distance[30].

Recently, theoretical solutions have been developed for transient ultrasonic fields using a variety of approaches including a Green's function technique[27-31]. The most applicable approach to this research is Hildebrand's[31] analysis of pulsed ultrasonic arrays. Beginning with a simple two-element array of one-dimensional circular apertures and assuming a spherical spreading factor, Hildebrand derived an expression for the impulse response of the array which is given below:

$$h(P_1, t) = \frac{c}{R_1 \sqrt{(\cos\theta - \cos\psi)^2 + 2\left(\frac{1}{R_1} + \frac{1}{R_0}\right)(ct - R_1)}} \times \text{rect} \left[ \frac{ct - R_1}{\frac{x^2}{2} \left(\frac{1}{R_1} - \frac{1}{R_0}\right) + x (\cos\theta - \cos\psi)} \right], \quad (6.1)$$

where  $c$  is the velocity of propagation and the remaining variables are shown in Figure 6.1. The field response at any point for a given input function may then be obtained by convolving the impulse response with the input function. For the case of a gated sine wave pulse, grating lobe suppression occurs due to the interference effect in the region of overlap of the pulses. Hence, the element spacing may be determined for no grating lobes given the input function and frequency.

Using a geometrical approach similar to Hildebrand's, a focusing piezoelectric transducer consisting of concentric ring electrodes was designed. This transducer design was incorporated in the design of an acoustooptical pulse-echo system. The motivation for the design of the overall system was the need for an electronically adjustable ultrasonic field in order to probe internal media structure and the ability to detect the reflected acoustic signal without

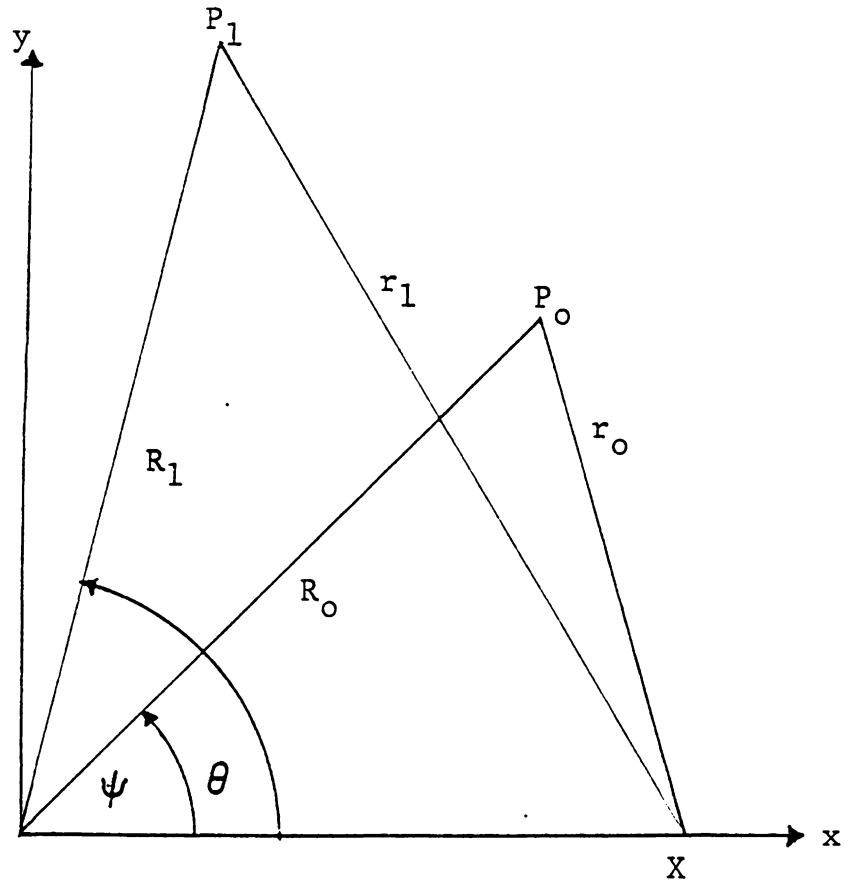


FIGURE 6.2: Two-element Focused Array Geometry[31]

loading the specimen surface at the measurement point[32]. The system design is complex and involves the integration of three sub-systems:

1. the ultrasonic sub-system,
2. the electrical sub-system, and
3. the optical sub-system.

The ultrasonic and electrical sub-systems are discussed in Chapter VII and are followed by a discussion of the optical sub-system and total system integration in Chapter VIII. The final chapter summarizes the work thus far and suggests further improvements and problems.

## Chapter VII

### TRANSDUCER AND ELECTRONIC SUBSYSTEM DESIGN

#### 7.1 ELECTRODE DESIGN AND FABRICATION

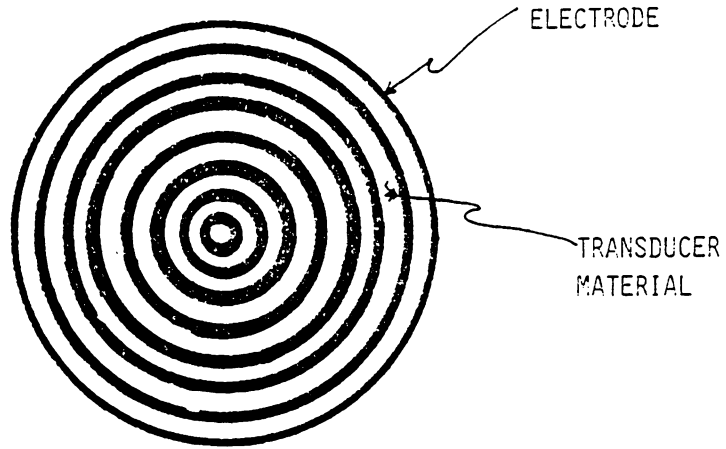
The transmitting transducer was fabricated from a circular 1.81 cm diameter x-cut 2.25 MHz quartz crystal substrate with a circular 1mm aperture in the center. Concentric ring electrodes were created on the upper surface of the transducer by depositing chrome-aluminum on the crystal, applying a mask using photographic transfer techniques and then etching away the unwanted metallic areas. The electrode configuration of the mask was determined with the aid of a FORTRAN computer program which is listed in Appendix C. The program took as inputs the transducer diameter, electrode spacing, electrode width, focal length, pulse repetition rate, and pulse width. From this information two tables were computed, examples of which are also contained in Appendix C. The first table listed the center-to-center ring spacings and the total number of rings. The second table listed the timing sequence for the requested focus length as well as the distance from each ring to the focus point and which rings were to be pulsed. From the data in the first table, a diagram of the electrode pattern was drawn and a negative

was made for the mask. The etching process required four steps, one step etching for the aluminum followed by a water bath and a second etching for the chromium followed by a final water bath. The chemical etchants are given in Appendix D.

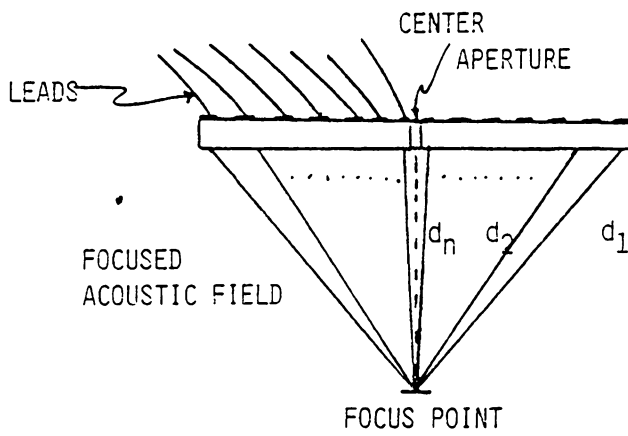
Leads for the transducer were made by stripping and filing #28 gauge wire down to a size smaller than the 0.028 cm diameter electrodes. The leads were attached to the electrodes using conducting epoxy thinned with ethanol. Figure 7.1.1 shows top and cross-sectional views of the transducer. To strengthen the lead-electrode bond, a layer of five-minute epoxy was added which also insulated the exposed leads and electrodes. Coaxial cables were then soldered to the leads and the transducer was mounted in a PVC tube to provide additional strain relief for the delicate leads. The bottom conducting surface of the transducer served as a ground plane.

## 7.2 ELECTRONIC PULSING CIRCUITRY

To achieve focusing, the transducer was operated in a pulsed mode which required that very fast-rising high-voltage pulses needed to excite the crystal be applied to the correct sequence of electrodes at the proper times. This



a.



b.

FIGURE 7.1.1: Transducer Electrode Configuration

requirement created a need for intricate timing of the pulses and also a need for high-power high-speed switching. Because high-speed switching is difficult at high-power levels, the pulse sequence was generated at a low power level and then amplified.

The amplifier circuit was designed and built next so that the response of one electrode ring could be examined. The circuit consisted of a complementary emitter follower level shifter feeding a high voltage FET switching transistor. Figure 7.2.1 shows the amplifier circuit; the resistor in parallel with the transducer was necessary to improve the turn-on time of the circuit. Figure 7.2.2 shows typical data from one electrode the lower trace shows the 200 V pulse output to the transducer and the upper trace shows the signal produced by the focusing transducer as detected by a uniform Panametrics 2.25 MHz transducer. Figure 7.2.2 emphasizes the severity of the switching problems encountered in this 'fast' circuit. The rise time of the circuit was not sufficient to excite the transducer so that the only excitation resulted on the falling edge of the pulse. While a faster switching circuit may be possible by using vacuum tubes, the high-voltage, high-speed requirement at low currents is pushing the present capabilities of high power FETs.

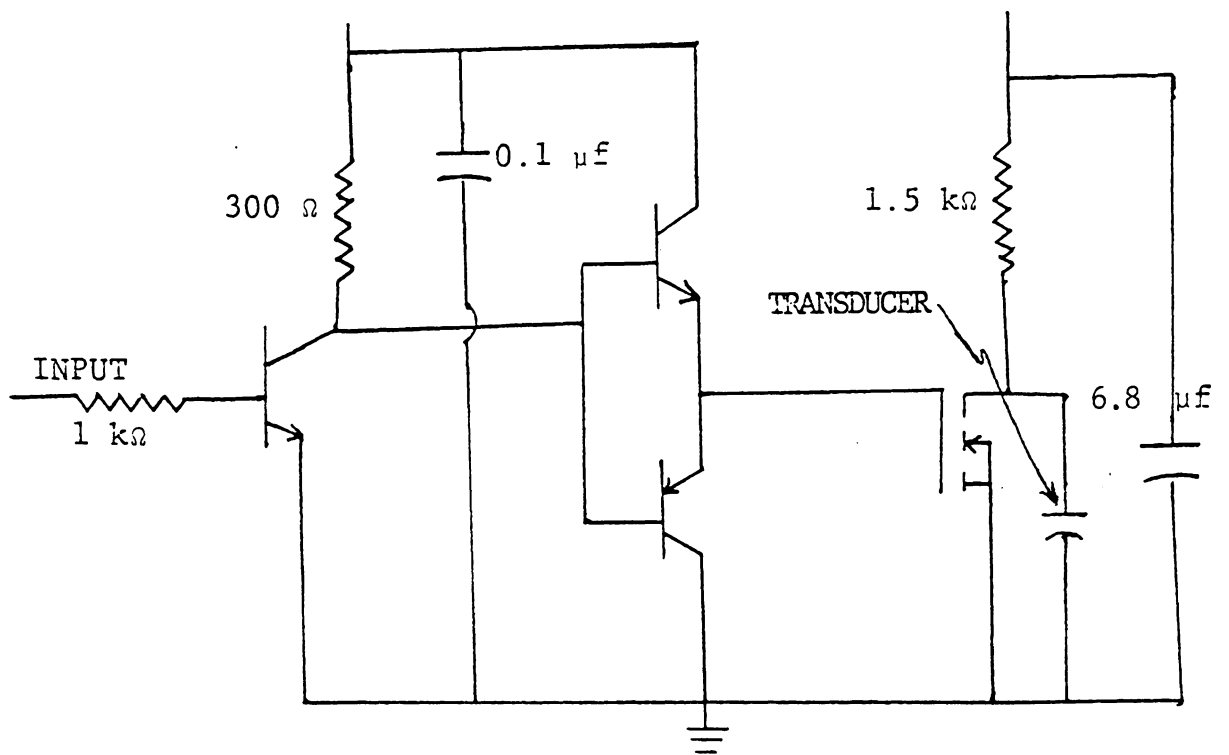


FIGURE 7.2.1: Voltage Amplifier Design

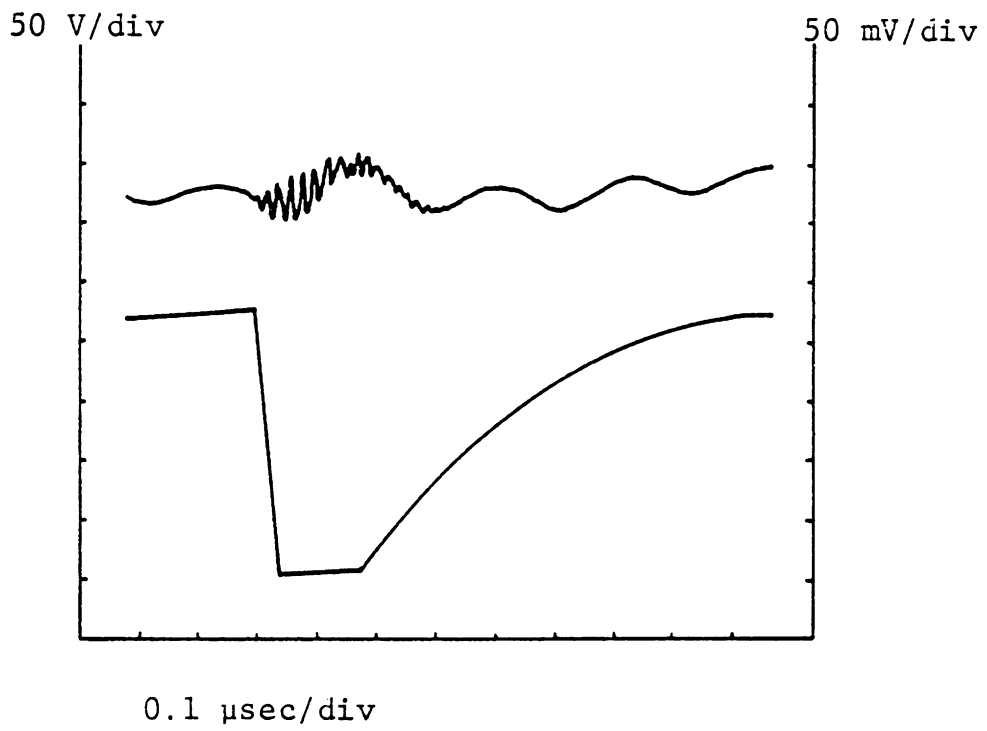


FIGURE 7.2.2: Acoustic Response of a Single Pulsed Ring

There are at least two possible design solutions for the low level pulsing circuit; the first one uses a complex microprocessor control but allows an adjustable pulse repetition rate and software control of focusing[32,33]. An external clock run by a frequency generator determines the pulse rate for a given application and the firing sequences for a particular focal length calculated in the program discussed previously are contained in look-up table form in the microprocessor memory. The user simply requests a focus length, pulse repetition rate, and whether the rings are to be pulsed once or repeatedly in the sequence required for focus; the microprocessor outputs the correct information to the rings and initiates the firing sequence.

Figure 7.2.3 shows a block diagram for this design. In this case not every ring will be pulsed for every focal length because the pulse repetition frequency must coincide with the phase delay required between rings for focus. This phase-pulse agreement will therefore limit the resolution of the focus spot and possibly the range of focal lengths allowed. The microprocessor controls a two-step process of first outputting the address sequence to the tri-state latches and then starting the clock that generates the low level image of the high voltage pulse after the data is sta-

ble in the tri-state latches. The microprocessor then gates the correct set of latches onto the address lines of demultiplexer 2 which selects the ring to be pulsed. Each of the sixteen outputs of the demultiplexer is tied to the input of the circuitry shown Figure 7.2.1. At the end of the sequence, the microprocessor prompts the user for further instructions or checks for a user-initiated interrupt if the repeated pulsing mode was requested.

A second design approach involves cascading 74123 retriggerable monostable multivibrators to obtain the correct phase timing for each electrode ring[34]. A low frequency clock generates a single pulse which is the input to a group of 74123s whose pulse lengths vary by the time delays required for particular rings. The output of each of these 74123s is the input to another 74123 whose output is the input to the circuitry in Figure 7.2.1. The phase variation between the pulses is thus determined by the external RC time constant of the first 74123. The information necessary to specify the method of focusing is the time-delay necessary for each ring and the associated resistor-capacitor combination required to achieve that time delay.

The second approach is less complicated conceptually; however, component tolerances for the small phase delays are

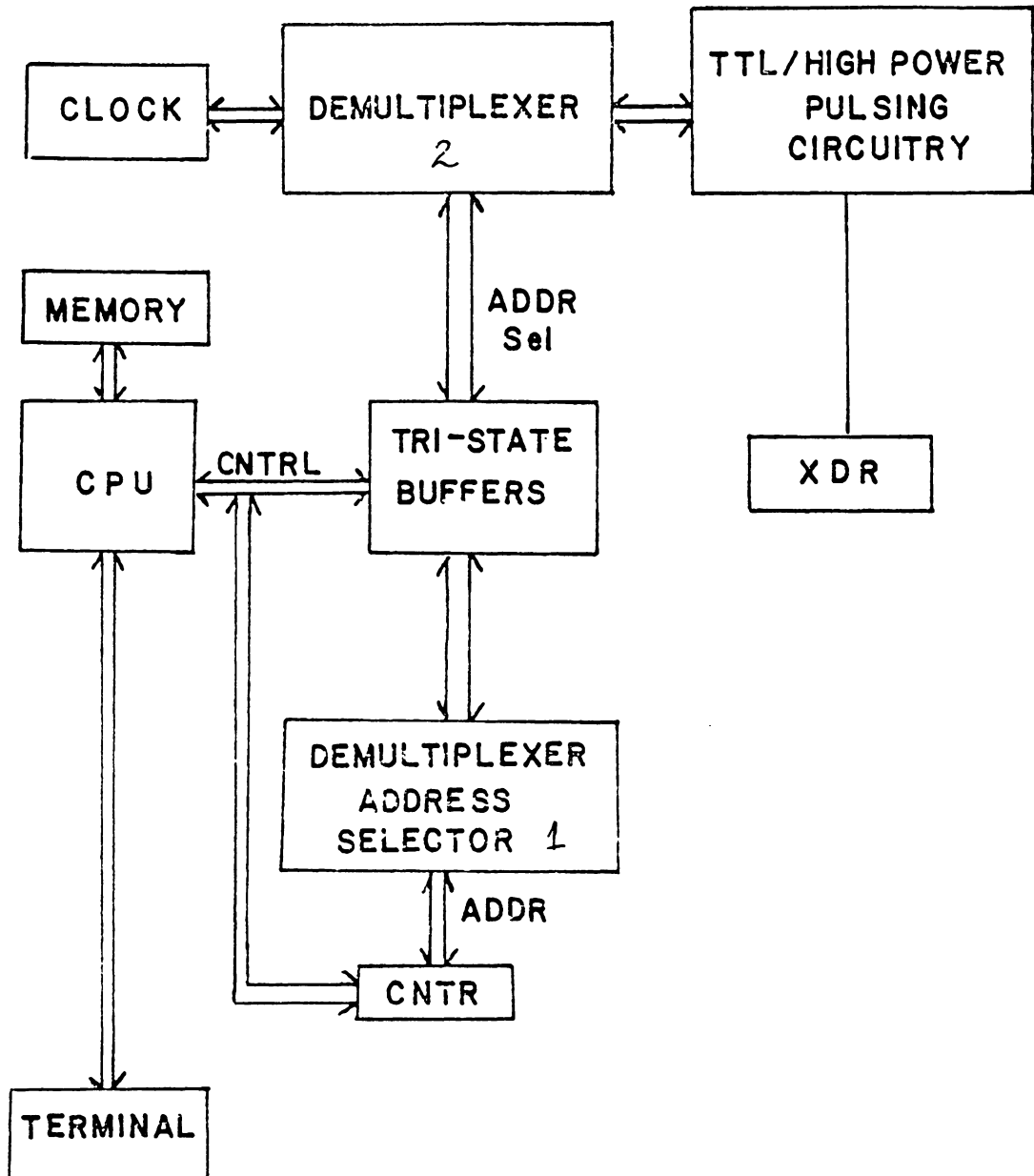


FIGURE 7.2.3: Block Diagram of Controller Electronics

critical and may limit the number of rings pulsed for a particular focus length. Each of the parallel circuits must have precision resistors and/or capacitors that must be adjusted manually each time the focus depth is changed. The microprocessor-controlled design requires critical timing considerations in the initial circuit design but allows the user more freedom once the circuit is implemented with less opportunity of error due to operator mistakes. An eight-bit microprocessor is limited to a maximum of sixteen rings, however, because of address decoding problems, whereas the cascaded 74123s may be paralleled without such a limit. In the end, the final design choice must be based on the flexibility required by the user.

## Chapter VIII

### OPTICAL DETECTION SYSTEM

The transducer and associated pulsing electronics discussed in Chapter VII may be used to generate a selectably focusable acoustic field. If the focused acoustic field is incident upon a bulk material anomaly at its focus point, the reflected field will propagate back to the transducer and produce a displacement of the free surface at the center of the transducer[32]. The normal component of surface displacement may be detected using the Michelson interferometer shown in Figure 8.1.1. The Michelson interferometer is very similar to the Mach-Zehnder interferometer discussed in Chapter III except the mechanism causing the modulation is at the end of the optical path rather than along the length of the path. Thus, the detailed theoretical analysis described in Chapter III also describes the operation of the Michelson interferometer.

#### 8.1 FEEDBACK STABILIZED MICHELSON INTERFEROMETER

In the Michelson interferometer shown in Figure 8.1.1, light from the monochromatic light source is split by the beamsplitter and focused on the surfaces of both a reference

mirror and the specimen. The reflected fields are then recombined by the beamsplitter and focused on an optical detector after being spatially filtered by a Ronchi ruling. The optical intensity modulation mechanism is shown explicitly in Figure 8.1.2 which is an enlarged view of the sample arm of Figure 8.1.1. The sub-surface anomaly reflects the focused incident acoustic field as shown. When the reflected bulk wave reaches the surface, mode conversion occurs and a surface wave results. The surface wave causes normal and parallel particle displacements in the free surface aperture area. The normal component of the particle displacement alters the path length of the sample arm which causes a phase shift in the optical field. As in the Mach-Zehnder interferometer, the phase shift causes a fringe shift which results in intensity modulation at the input of the optical detector. Thus, the resulting electrical signal at the output of the detector is proportional to the normal component of surface motion.

## 8.2 FEEDBACK STABILIZATION OF THE MICHELSON INTERFEROMETER

The Michelson interferometer is inherently sensitive to environmental noise which can inundate the small signals created by the surface particle displacements. To eliminate

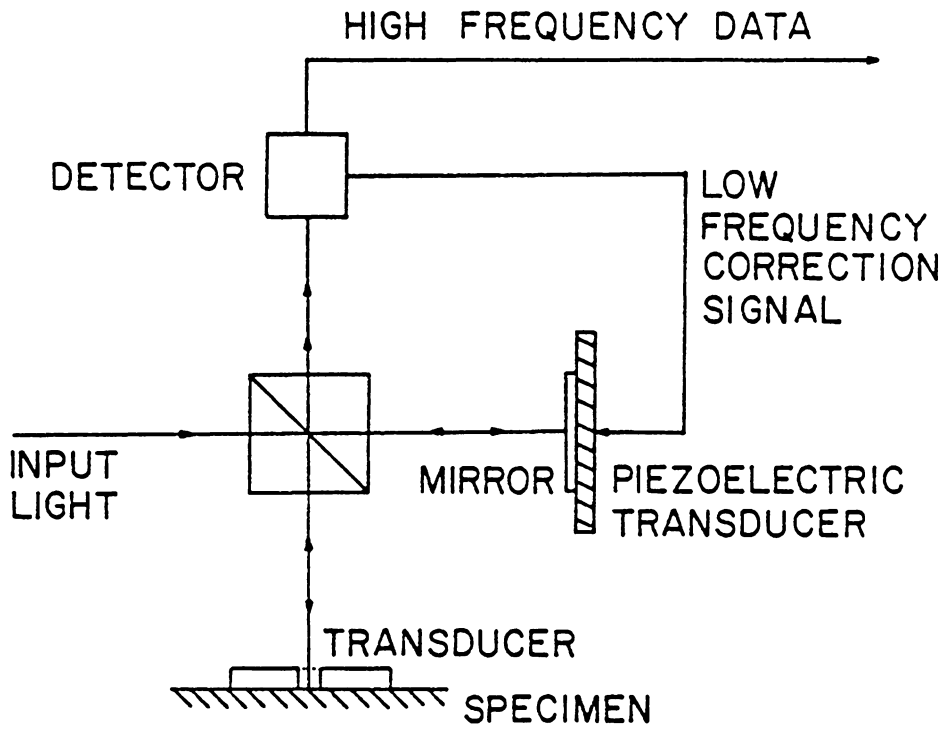


FIGURE 8.1.1: Feedback Stabilized Michelson Interferometer

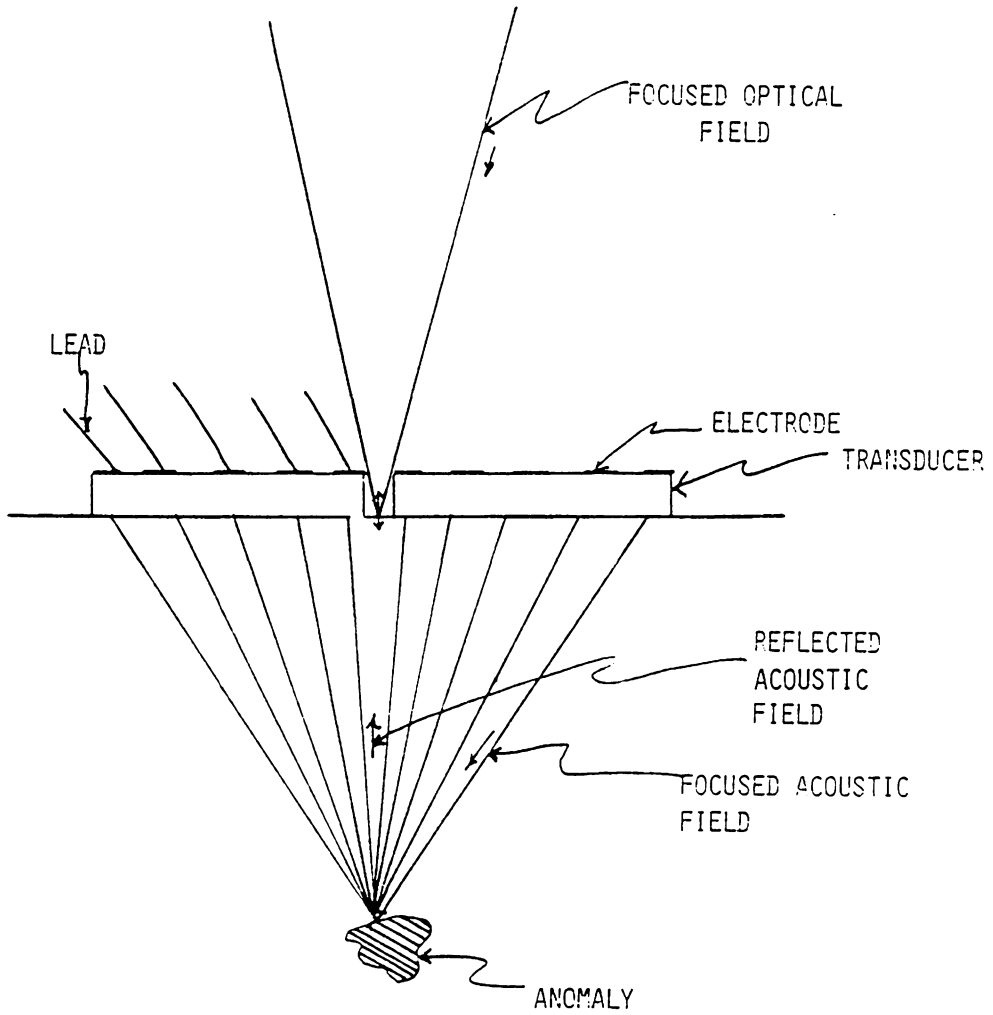


FIGURE 3.1.2: Optical Detection of the Reflected Acoustic Field

the low frequency noise components, the reference mirror may be mounted on a piezoelectric translation stage rather than a stationary mount. This piezoelectric transducer is then fed with an amplified low frequency signal from the detector. Additionally, the feedback correction circuit fixes the gain of the interferometer and may therefore be adjusted to maximize the gain. This feedback technique has non-linear stability problems because the voltage compensation cannot be made infinite; however, it enables system operation in acoustically hostile environments.

## Chapter IX

### ACOUSTOOPTICAL PULSE-ECHO SYSTEM SUMMARY

The generation of a focused acoustic field using a pulsed concentric electrode array transducer has been examined. The focusing phenomena is based on the geometric superposition of the pulsed fields from each of the rings at the point and time in space where the fields interact. The focused field may be used as a point probe to interrogate internal media structure which enables the tomographic reconstruction of the acoustic impedance field of the medium. Internal media reconstruction is possible because the energy in the reflected wave is determined by the reflection coefficient of the medium at the focus point. Variation in the reflection coefficients due to material anomalies and voids cause an energy variation which may be used to infer material shapes. The feedback stabilized optical receiving transducer detects the normal component of surface displacement which results as the reflected energy strikes the surface. The system has applications in materials characterization of both human tissues and organs as well as manmade materials because of the non-invasive nondestructive nature of the point probing technique.

The design of the three sub-systems has been discussed and total system integration has been outlined. The design of each sub-system has created a need for further research in some problem areas. Solutions to these problems would eliminate some of the stringent system requirements. For example, to improve transducer efficiency, impedance matching circuitry for the transducer could be designed and implemented once a detailed model of the single substrate concentric ring array was developed. This not only requires a thorough knowledge of the crystal response, but also requires more sophisticated equipment for impedance measurement than is available presently at Virginia Tech. Another method of improving transducer efficiency is to use a more robust piezoelectric material such as PZT or lithium niobate in the transmitting transducer. If either or both of these ideas were incorporated into the transmitting transducer design, the high-voltage pulse requirement would be reduced, consequently reducing the associated electronics problems. In addition, the resolution of the focus spot might be increased because of the resulting sharper input pulse. As mentioned previously, vacuum tubes may also provide a faster rise time in the pulsing circuit. Another alternative to vacuum tubes may be using an SCR circuit which could improve the rise time[32].

The design of the microprocessor-controlled focusing system is highly complex and requires a very intricate timing interface because of the small phase delays between inter-ring pulses. However, the flexibility of the final control creates some intriguing possibilities. Pulse amplitude variation as well as phase variation could easily be achieved using the microprocessor system so the resolution of the focus could be maximized for any given focal length. Because the focus is determined by a convolution of the step response of the system and the input function, the space and time evolution of input fields may be determined. Therefore, for a desired field at the focus position, the required amplitude and phase of the input field function could be calculated and programmed into the system. The abundant potential of the software-controlled system clearly indicates its superiority over the monostable multivibrator control.

Finally, the ability to ultrasonically point probe a specimen presents a new challenge in the field of ultrasonic characterization of materials. The technique presented in this thesis is the first to integrate an optical detection transducer with an ultrasonic transmitting transducer to produce a system that can generate and detect a focused

acoustic field. The system presents a challenging alternative to present nondestructive evaluation methods but demands a further understanding of flaw characterization as well as improved data interpretation and analysis.

## REFERENCES

- [1] W. Sachse and N. N. Hsu, 'Ultrasonic transducers for materials testing,' Physical Acoustics XIV, W. P. Mason and R. N. Thurston eds., New York: Academic Press, 1979.
- [2] M. J. Howes and D. V. Morgan, eds., Optical Fibre Communications, Chichester: John Wiley and Sons, 1980.
- [3] H. F. Wolf, ed., Handbook of Fiber Optics, New York: Garland Pub. Inc., 1979.
- [4] Fiber/Laser News, 2, Washington D. C., ISSN 0275-6099, March 5, 1982.
- [5] T. G. Giallorenzi, 'Fiber-optic sensing of pressure and temperature,' Optics and Laser Technology 13, 73, (1982).
- [6] G. B. Hocker, 'Fiber-optic sensing of pressure and temperature,' Appl. Optics 18, 1445, (1979)
- [7] V. Vali and R. Shorthill, 'Fiber ring interferometer,' Appl. Opt., 15, 1099 (1976).
- [8] J. A. Bucaro, H. D. Dardy, and E. F. Carome, 'Fiber-optic detection of sound,' Appl. Opt. 16, 1961 (1977).
- [9] J. A. Bucaro and E. F. Carome, 'Single fiber interferometric acoustic sensor,' Appl. Opt. 17, 330 (1978).
- [10] J. H. Cole, R. L. Johnson, and P. G. Bhuta, 'Fiber-optic detection of sound,' J. Acoust. Soc. Am. 62, 1136 (1977).
- [11] D. Marcuse, Light Transmission Optics, New York: Van Nostrand Reinhold Co., 1972
- [12] F. A. Jenkins, H. E. White, Fundamentals of Optics, New York: McGraw Hill, 1976.
- [13] J. C. Wade, P. S. Zerwekh, and R. O. Claus, 'Detection of acoustic emission in composites by optical fiber interferometry,' Proc IEEE Ultrasonics Symp. 2, 849 (1981).

- [14] D. P. Jablonowski, 'Simple interferometer for monitoring Rayleigh waves,' Appl. Opt. 17, 2064 (1978).
- [15] R. O. Claus and J. H. Cantrell, 'Detection of ultrasonic waves in solids by an optical fiber interferometer,' Proc. IEEE Ultrasonics Symp. 2, 719 (1980).
- [16] C. H. Palmer and R. O. Claus, 'Ultrasonic wave measurement by differential interferometry,' Appl. Opt. 16, 1849 (1977).
- [17] A. C. Ugural, Stresses in Plates and Shells, New York: McGraw Hill, 1975.
- [18] J. N. Reddy, personal communication, Engineering Science and Mechanics Department, V. P. I. & S. U., April 1982.
- [19] A. E. Lord, Jr., 'Acoustic Emission,' in Physical Acoustics XI, W. P. Mason and R. N. Thurston, eds., Academic Press: New York, 1975.
- [20] D. M. Morse and K. V. Ingard, Theoretical Acoustics, New York: McGraw Hill, 1968.
- [21] S. N. Rzhevikin, A Course of Lectures on the Theory of Sound, New York: Macmillian Co., 1963.
- [22] R. Crane, 'Fiber optics for a damage assesment system for fiber reinforced plastic composite naval structures,' ARO/DARPA Workshop on Nondestructive Evaluation of Polymers and Polymer-based Composites, (Wrightsville Beach, N. C.), April 1982.
- [23] R. Crane, 'Fiber optics for a damage assesment system for fiber reinforced plastic composite structures,' AF/DARPA-NAVY/DARPA Review of Progress in Quantitative NDE (SanDiego, CA), August 1982.
- [24] W. P. Mason, Piezoelectric Crystals and Their Applications to Ultrasonics New York: D. Van Norstrand Co., 1964.
- [25] B. A. Auld, Acoustic Waves in Solids: Volume I New York: John Wiley and Sons, 1973.

- [26] L. Filipczynski and J. Etienne, 'Theoretical study and experiments on spherical focusing transducers with Gaussian surface velocity distribution,' *Acustica* 28, 121 (1973).
- [27] L. D. Lukker, A. L. VanBuren, M. D. Jwnager, and A. C. Tims, 'Experimental constant beamwidth transducer,' *J. Acoust. Soc. Am. Suppl. 1*, 71, (1982).
- [28] P. R. Stephanishen, 'Impulse response and radiation impedance of an annular piston,' *J. Acoust. Soc. Am.* 56, 305 (1974).
- [29] A. Penttinen and M. Luukkala, 'The impulse response and pressure nearfield of a curved ultrasonic radiator,' *J. Phys. D: Appl. Phys.* 9, 1547 (1976).
- [30] Y. A. Kondrat'ev, 'Pulsed operation of a focusing piezoelectric transducer,' *Soviet J. of Nondestructive Testing* 14, 688 (1978).
- [31] B. P. Hildebrand, 'An analysis of pulsed ultrasonic arrays,' in *Acoustical Holography VIII*, A. F. Metherell, ed. New York: Plenum Press (1980).
- [32] J. C. Wade, and R. O. Claus, 'Acoustooptical pulse-echo transducer system,' *Proc. Southeastern Sym. on System Theory*, 14, 163 (1982).
- [33] J. C. Wade and R. O. Claus, 'Interferometric pulse-echo ultrasonic transducer system,' *J. Acoust. Soc. Am.*, 71, s109 (1982).
- [34] R. O. Claus and J. C. Wade, Invited paper, *J. Acoust. Soc. Am.*, to be submitted.
- [35] L. Burgess, personal communication, PhD. candidate, Chemistry Department, V. P. I. & S. U., April 1982.
- [36] L. I. Massil and R. Glang, eds., Handbook of Thin Film Technology, New York: McGraw Hill, 1970.

## BIBLIOGRAPHY

- J. A. Bucaro and E. F. Carome, 'Single fiber interferometric acoustic sensor,' Appl. Opt. 17, 330 (1978).
- R. A. Cline, R. E. Green, and C. H. Palmer, 'A comparison of optically and peizeoelectrically sensed acoustic emission signals,' J. Acoust. Soc. Am. 64, 1633 (1978).
- R. E. Collin and F. J. Zucker, Antenna Theory: Part 2, New York: McGraw Hill, 1969.
- S. Lees, 'Useful criteria in describing the field pattern of focusing transducers,' Ultrasonics 16, 229 (1978).
- H. T. O'Neil, 'Theory of focusing radiators,' J. Acoust Soc. Am., 21, 516 (1949)
- S. C. Rashleigh, 'Magnetic-filed sensing with a single-mode fiber,' Optics Letters 6, 19 (1981).
- G. A. Rines, 'Fiber-optic accelerometer with hydrophone applications,' Appl. Opt. 20, 3453 (1981).
- D. E. Robinson, and S. Lees, L. Bess, 'Near field transient radiation patterns for circular pistons,' IEEE Trans on Acoust. Speech, and Signal Processing, 22, 395 (1974).
- S. Silver, Microwave Antenna Theory and Design, Dover Publications: New York, 1965.
- J. VanRoey, J. van der Donk, and P. E. Lagasse, 'Beam-propagation method: analysis and assessment,' J. Opt Soc. Am. 71, 803, (1981).
- A. D. Vopilkin, et. al. 'Wide-band ultrasonci transducer and its uses,' United States Patent #3968680, July 1976.
- G. W. Willard, 'Focusing ultrasonic radiators,' J. Acoust. Soc. Am., 21, 360 (1949).
- P. S. Zerwekh and R. O. Claus, 'An ultrasonic transducer with Gaussian radial velocity distribution,' IEEE Ultrasonics Sym. 2, 974 (1981).

## Appendix A

### PREPARING OPTICAL FIBERS FOR USE IN AN INTERFEROMETER

In any optical fiber interferometric experiment, the most critical part of experimental preparation is the preparation of the optical fiber. If the fiber is cut incorrectly, the numerical aperture will be distorted and the incident light will not propagate down the fiber. The fiber must be stripped and cleaved so that both the input and output ends of the fiber are perpendicular to the fiber axis and free of debris such as dust or dirt. There are two ways to strip an optical fiber; one is with a very sharp razor blade and the other is with a chemical process[36]. The razor blade method is straightforward:

1. Hold the fiber about six inches from the end to be stripped.
2. Place the fiber on a smooth, hard, and flat surface.
3. Nick the fiber jacket and gently apply pressure on the fiber with the razor blade while pulling the fiber out from under the blade.

4. Repeat until the jacketing and RTV are removed from the entire circumference of the fiber.

The key to success with this method is to have a sharp blade with no ruts or nicks that will grab the fiber and break it. This method is best when short lengths of bare fiber are needed.

The second method is a chemical process[35] that requires good ventilation and time. However, it is the only practical way to strip long lengths of fiber because maintaining even pressure on the fiber is extremely difficult for long lengths. The chemical process is a two-step process; the first step removes the outer jacket while the second step removes the inner Hytrel® layer.

1. Heat nitrobenzene to 100° C and place the fiber in the heated solution for about 1 hour or until all the Hytrel® is removed.
2. Rinse in ethanol until the silicone polymer coating becomes clear.
3. Place the fiber in a 5% solution of potassium hydroxide and ethanol (5g KOH to 100 ml ethanol) for 2-3 hours until the silicon rubber beads up.

4. Remove the fiber and carefully strip the beads off the fiber with your fingers or a razor blade.
5. Soak about 10 minutes more.
6. Rinse with H<sub>2</sub>O.

Once the fiber is stripped the ends must be cleanly cut. There are two methods of cutting the fiber as well. The most repeatably reliable method of cleaving the fiber is by using the fiber cutter shown in Figure A1.1; however, each time the fiber is cut approximately 4 inches of the fiber is lost. This method is outlined below:

1. Push the sliding chock the wedge until the wedges touch as shown in Figure A1.1.
2. Place the fiber on the wedges and secure the clamps shown in Figure A1.1.
3. Slide the chock out from under the wedge until the fiber is taut.
4. Gently lower the diamond scribe cutter on the balance bar above the wedge until it rests on the fiber.

5. Translate the scribe across the fiber until the fiber breaks by adjusting thumbscrew in Figure A1.1.
6. Examine the end under a microscope to be sure that no splinters are left on the sides and that the cut is perpendicular to the fiber axis.

The second method is the economy method for use when fiber lengths are short:

1. Tape approximately 0.5 to 1 cm of the fiber to a hard surface.
2. Hold the fiber near the taped end so that it is under tension.
3. Scribe the fiber with a diamond scribe while maintaining tension on the fiber until the crack created by the scribe causes the fiber to break.
4. Check the fiber as in '5' above. Before the fiber is used in the experimental system, apply an index matching mode stripping fluid to approximately 0.5 cm of the fiber.

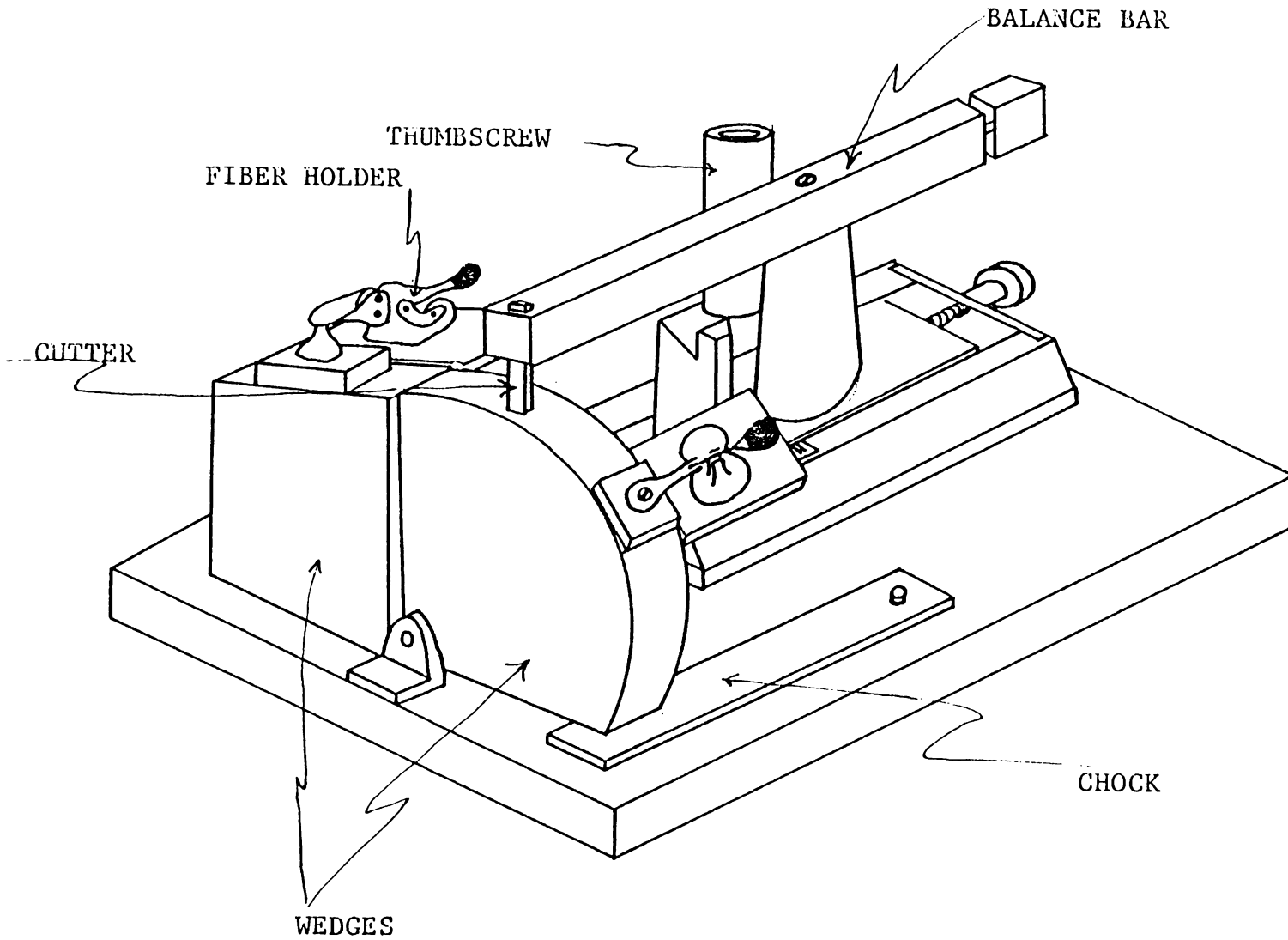


FIGURE A1.1: Optical Fiber Cutter

## Appendix B

### STRAIN DATA AND CALCULATIONS

The calibration data were taken using a Houston Instruments x-y plotter connected to the output of the detector. Typical data are shown Figure A2.1. The data shows the fringe shifts corresponding to the pathlength changes which occur as the fibers undergo tension or compression. The number of fringes for a given strain  $\epsilon$  is then:

$$N = \epsilon / \lambda, \quad (\text{A2.1})$$

where  $\epsilon$  is given by:

$$\epsilon = 3da/4L$$

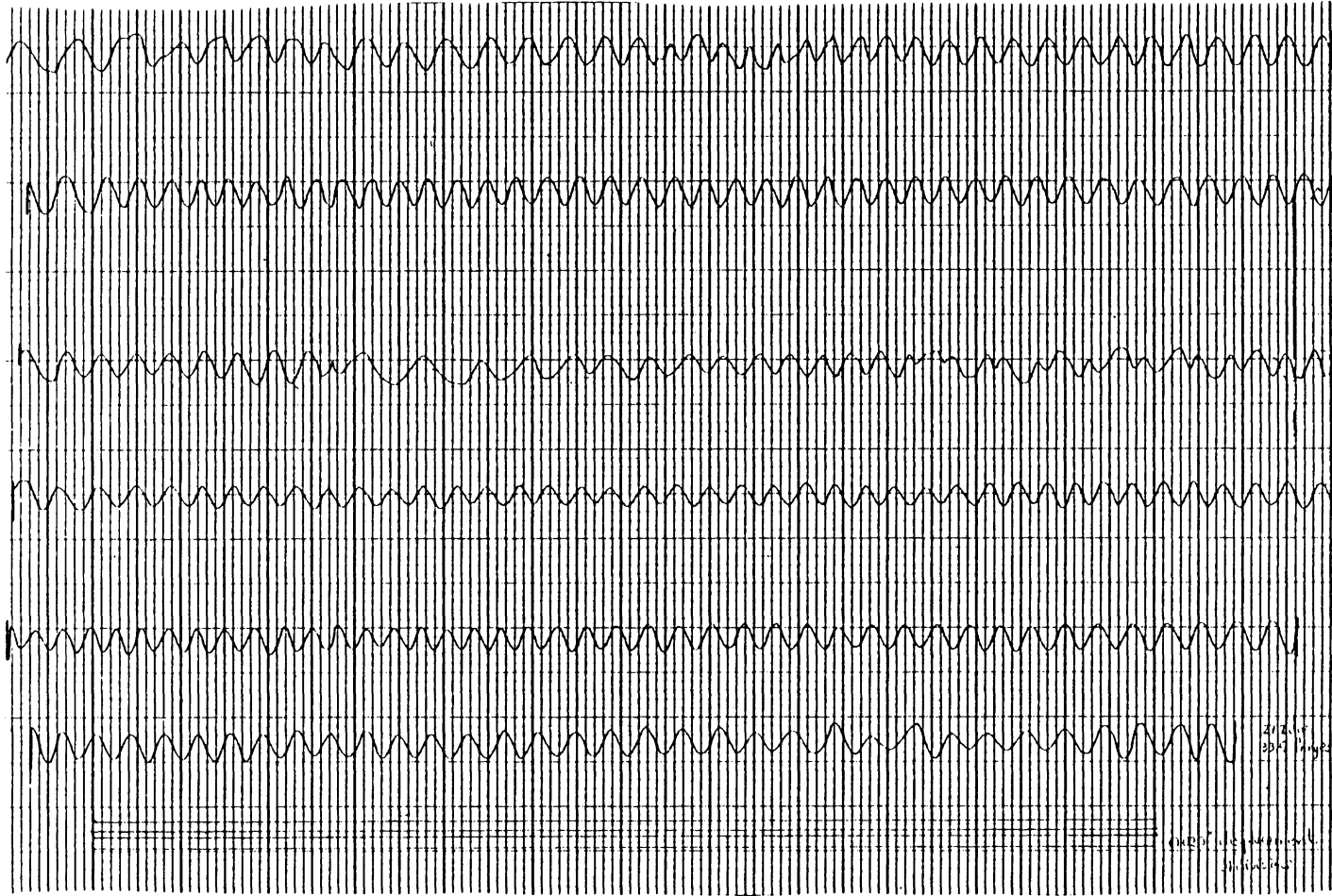
where  $d$ ,  $a$ , and  $L$  are the dimensions of the cantilever beam as indicated in Figure 3.3.1 of Chapter III. Thus for given beam dimensions, the theoretical strain may be calculated and compared to the number of fringes counted during a calibration interval. For example using the data in Figure A2.1,  $N=29.73$ . Calculating the strain from the dimensions given in the figure title,

$$\varepsilon = 6.27 \times 10^{-4} \quad (\text{A2.1}).$$

The monochromatic source was a helium-neon laser whose wavelength is 6328 Å. Thus

$$N = \varepsilon / \lambda = 29.73, \quad (\text{A2.3})$$

which yields an experimental error of 10%.



$d=0.05$  cm  $a=0.32$  cm  $L=25,72$  cm

FIGURE B1.1: Strain Calibration Data

## Appendix C

### FORTRAN PROGRAM FOR CALCULATING TRANSDUCER VARIABLES

The program listed below was used to calculate the transducer variables prior to the etching process. Typical data is shown in Table A3.1 for a 7.5 cm transducer with a focal length of 5 cm, a pulse repetition rate of 1.5 MHz and electrode spacings of 0.001 cm.

```
C
C THIS PROGRAM CALCULATES THE NECESSARY PARAMETERS NEEDED TO DET-
C ERMINE THE FIRING SEQUENCE OF THE RINGS OF A CIRCULAR
C TRANSDUCER GIVEN THE DIAMETER OF THE TRANSDUCER, THE WIDTH OF
C THE RING, THE SPACING BETWEEN THE RINGS, THE PULSE FREQUENCY
C AND WIDTH, AND THE FOCAL LENGTH
C
C
C THE INPUT VARIABLES ARE:
C
C D=DIAMETER OF THE TRANSDUCER IN MILS
C W=WIDTH OF THE RINGS TO BE DEPOSITED IN MILS
C S=SPACING BETWEEN RINGS IN MILS
C F=PULSE FREQUENCY
C PW=PULSEWIDTH
C C=MINIMUM DIAMETER OF THE CENTER SPOT IN MILS
C LO=FOCAL LENGTH
C TOL=TOLERANCE OF THE TIMING PULSE IN SECONDS
C
C
C OTHER CALCULATED VARIABLES INCLUDE
C
C SP=CALCULATED CENTER TO CENTER RING DISTANCE
C CF=CONVERSION FACTOR FROM CM TO MILS
C VWC=SPEED OF SOUND IN MEDIUM IN CM.
      DIMENSION DR(50),TH(50),L(50),T1(50),TN(50),P(50),R(50),
1 RP(50),PR(50)
      REAL DR,TH,L,T1,TN,P,RP,PR,D,W,S,F,PW,C,LO,TOL
      READ (5,*) D,W,S,F,PW,C,LO,TOL
C CALCULATE THE RADIUS OF THE TRANSDUCER IN CM
      R(1)=((D-30)/2000)*2.54
```

```

C CALCULATE THE CENTER TO CENTER DISTANCE OF THE RINGS
  SP=(S/1000)*2.54+(W/1000)*2.54
  I=1
C CONVERT MINIMUM DIAMETER FROM MILS TO A RADIUS IN CM
  C=(C/2000)*2.54
  VWC=1430*100
  RP(1)=0
  TN(1)=0
  T1(1)=0
  P(1)=0
  TP=1/(2*F)
  IF (TP .GT. PW) GOTO 100
  PRINT 50
50 FORMAT ('0','THIS FREQUENCY AND PULSEWIDTH ARE NOT
1 COMPATIBLE.')
  GOTO 5000
100 PRINT 105
105 FORMAT ('1','THE CENTER LOCATION OF EACH RING IN CM
1 AND MILS ARE GIVEN BELOW.')
  PRINT 110
110 FORMAT ('0',5X,'R(CM)', 15X, 'R(MILS)',9X, 'R-C (CM)')
115 IF (R(I) .LE. C) GOTO 200
  RP(I)=(R(I)/2.54)*1000
  PRINT 130, R(I),RP(I),R(I)-C
130 FORMAT ('0',5X, F10.4,5X,F10.4, 5X, F10.4, 5X, F10.4)
CCALCULATE THE NEXT LOCATION
  R(I+1)=R(I)-SP
  I=I+1
  GOTO 115
200 PRINT 205,I-1
205 FORMAT ('0','THE NUMBER OF RINGS IS I=',I3)
  PRINT 300
300 FORMAT ('1', 'THE PULSING SEQUENCE DATA IS GIVEN BELOW')
  PRINT 310, LO,D,I-1,F,PW
310 FORMAT ('0',F14.4,2X,F14.4,2X,I3,2X,E14.7,2X,E14.7)
  PRINT 320
320 FORMAT ('0',5X,'R(CM)', 15X, 'TH',15X, 'LO',15X,'T1',
1 10X,'P',10X,'PR')
  J=I-1
  DO 520 N=1,J
  TH(N)=ATAN(R(N)/LO)
  L(N)=R(N)/SIN(TH(N))
  IF (N .EQ. 1) GOTO 380
  TN(N)=(L(N-1)-L(N))/VWC
  T1(N)=(L(1)-L(N))/VWC
355 IF (P(N) .GT. T1(N)+TOL) GOTO 400
  IF (P(N) .LT. T1(N)-TOL) GOTO 390
380 PR(N)=1

```

```
GOTO 450
390 P(N)=P(N)+1/F
395 GOTO 355
400 PR(N)=0
450 R (N+1)=R(N)-SP
500 P(N+1)=P(N)
    PRINT 510 ,R(N),TH(N),L(N),T1(N),P(N),PR(N)
510 FORMAT ('0',5X,F10.4,3X,F10.4,3X,F10.4,3X,E14.7,3X,
1 E14.7,3X,F10.4)
520 CONTINUE
5000 STOP
    END
3000,50,50,1.50E6,150E-9,50,5,50E-9
```

TABLE A1.1

Center Ring Locations for a Typical Transducer

R(CM)	R(MILS)	R-C (CM)
3.7719	1484.9980	3.7084
3.5179	1384.9980	3.4544
3.2639	1284.9970	3.2004
3.0099	1184.9980	2.9464
2.7559	1084.9980	2.6924
2.5019	984.9978	2.4384
2.2479	884.9976	2.1844
1.9939	784.9973	1.9304
1.7399	684.9971	1.6764
1.4859	584.9968	1.4224
1.2319	484.9966	1.1684
0.9779	384.9966	0.9144
0.7239	284.9966	0.6604
0.4699	184.9967	0.4064
0.2159	84.9967	0.1524

THE NUMBER OF RINGS IS I= 15

TABLE A2.2

## Firing Sequence Data

R(CM)	LO	T1	P	PR
3.772	6.263	0.0000E 00	0.0000E 00	1.0000
3.518	6.114	0.1046E-05	0.1333E-05	0.0000
3.264	5.971	0.2043E-05	0.2000E-05	1.0000
3.010	5.836	0.2987E-05	0.3333E-05	0.0000
2.756	5.709	0.3874E-05	0.4000E-05	0.0000
2.502	5.591	0.4700E-05	0.4667E-05	1.0000
2.248	5.482	0.5462E-05	0.6000E-05	0.0000
1.994	5.383	0.6156E-05	0.6667E-05	0.0000
1.740	5.294	0.6777E-05	0.7333E-05	0.0000
1.486	5.216	0.7322E-05	0.7333E-05	1.0000
1.232	5.149	0.7788E-05	0.8000E-05	0.0000
0.978	5.095	0.8171E-05	0.8667E-05	0.0000
0.724	5.052	0.8469E-05	0.8667E-05	0.0000
0.470	5.022	0.8679E-05	0.8667E-05	1.0000
0.216	5.005	0.8801E-05	0.9333E-05	0.0000

Appendix D  
CHEMICAL ETCHANTS

The chemical etchants listed below are given in the Handbook of Thin Film Technology[36].

1. Aluminum: The primary etchant is a 20% solution of Sodium Hydroxide (NaOH); however this proved unsatisfactory because of severe undercutting as well as severe degradation of the adhesion properties of the KPR3 photoresist. A better etchant is Ferric Chloride.
  
2. Chromium: The primary etchant is alkaline ferricyanide:
  - a) 1 part of a solution of 50 g NaOH
  
  - b) 100 ml deionized water plus
  
  - c) 3 parts of a solution of 100 g  $K_3[Fe(CN_6)]$  and 300 ml of deionized  $H_2O$ .
  
  - d) Dissolve  $K_3[Fe(CN_6)]$  by heating  $H_2O$  slightly and stirring constantly

- e) Remove from heat and add NaOH.
3. Gold: the primary etchant is aqua regia:
- a) 1 part concentrated HCl
  - b) 3 parts  $\text{HNO}_3$ .
4. However, this etchant is so highly reactive that it removes the photoresist as well and is therefore, unsatisfactory.
5. An alternative etchant that is much less caustic is potassium iodide (KI) and iodine ( $\text{I}_2$ ):
- a) 400 g KI
  - b) 100 g  $\text{I}_2$
  - c) 400 ml deionized  $\text{H}_2\text{O}$ .
  - d) Heat deionized  $\text{H}_2\text{O}$  slightly and stir in KI and  $\text{I}_2$  until everything is dissolved.

The photoresist used in all cases was KPR3 because of its availability, despite the fact that it is not listed as the preferred photoresist on either the aluminum or gold. The photoresist worked best when mixed 50-50 with the KPR3 sol-

vent and post-baked for 15-20 minutes at 150<sup>0</sup> F. The post-bake temperature should not exceed 150<sup>0</sup> F as the photoresist is more difficult to remove the higher the post-bake temperature.

Etch the metal by pouring a small amount of the proper etchant into a glass dish and immerse the transducer in the etchant, while gently moving the dish to agitate the etchant as it passes over the transducer. The etching process should be checked frequently by rinsing the transducer periodically and visually examining it to see if the undesired metal is removed. Over-etching will cause undercutting of the rings.

**The vita has been removed from  
the scanned document**

ACOUSTOOPTICAL TECHNIQUES FOR ULTRASONIC MATERIALS  
EVALUATION:  
OPTICAL FIBER INTERFEROMETRY AND PULSE-ECHO SYSTEMS

by

Janet Christiana Wade

(ABSTRACT)

The performance of two acoustooptical systems for ultrasonic materials characterization has been investigated. The first system uses an optical fiber interferometric technique to detect directly slowly varying residual stresses and both high frequency continuous and transient ultrasonic waves characteristic of acoustic emission events in composites. The potential for embedding optical fibers inside fiber composites during manufacturing makes this an attractive built-in alternative to conventional contact transducers for the nondestructive evaluation of composite materials. Experimental static and dynamic calibration as well as the frequency domain characterization of acoustic emission as detected by this system are discussed.

The second system is a pulse-echo transducer system that generates an electronically focusable ultrasonic field and

detects the reflected field optically. The generating transducer consists of concentric ring electrodes etched on a single x-cut quartz crystal substrate with a 1 mm circular aperture at the center. By shaping the amplitude and phase profile of the high voltage pulse applied to each ring, a focused ultrasonic field results at an adjustable distance below the transducer. If the field is focused below the surface of a specimen, energy in the wave reflected from the focal point modulates the normal and parallel components of surface displacement. Furthermore, if the sample arm of an adaptively stabilized interferometer is focused on the free surface at the transducer center aperture, the normal component of surface motion may be detected. This system has potential applications in materials characterization and evaluation as well as biomedical imaging. The design of the system is discussed with particular emphasis on the necessary sub-system interfaces required for operational flexibility.